Grain Orientation, Angle of Incidence, and Beam Polarization Effects on Ultraviolet 300 ps-Laser-Induced Nanostructures on 316L Stainless Steel

Luis Porta-Velilla, Elena Martínez, Alejandro Frechilla, Miguel Castro, Germán Francisco de la Fuente, Jörn Bonse, and Luis Alberto Angurel*

Laser-induced periodic surface structures (LIPSS) represent a unique route for functionalizing materials through the fabrication of surface nanostructures. Commercial AISI 316L stainless steel (SS316L) surfaces are laser treated by ultraviolet 300 ps laser pulses in a laser line scanning (LLS) approach. Processing parameters are optimized (pulse energy of 2.08 µJ, pulse repetition frequency of 300 kHz, and suitable laser scan and sample displacement rates) for the generation of low spatial frequency LIPSS over a large 25 × 25 mm² area. Different angles of incidence of the laser radiation (0°, 30°, and 45°) and different linear laser beam polarizations (s and p) produce a plethora of rippled surface morphologies at distinct grains. Scanning electron microscopy and 2D Fourier transforms, together with calculations of the optical energy deposited at the treated surfaces using Sipe's first-principles electromagnetic scattering theory, are used to study and analyze in detail these surface morphologies. Combined with electron backscattering diffraction, analyses allow associating site-selectively various laser-induced-surface morphologies with the underlying crystalline grain orientation. Resulting grain orientation maps reveal a strong impact of the grain crystallographic orientation on LIPSS formation and point toward possible strategies, like multi-step processes, for improving the manufacturing of LIPSS and their areal coverage of polycrystalline technical materials.

1. Introduction

AISI 316L stainless steel (SS316L) is a chromium-nickel-molybdenum austenitic (non-magnetic) stainless steel. The low carbon content (<0.03%) improves the intergranular corrosion properties,[1] whereas the presence of molybdenum in the passive layer improves the resistance to pitting corrosion.[2] Due to its great corrosion resistance, this alloy is used for applications in a wide range of fields, including marine, chemistry, food processing, and biomedicine equipment. Considering this last field and despite being less biocompatible than Co-Cr-Mo- and Ti-alloys, the SS316L is one of the most used materials in biomedicine due to its lower costs. Even if metallic biomaterials are able to resist highly corrosive environments, they are inert materials whose surfaces must usually be modified in order to improve their biocompatibility.[1,3,4,5] Moreover, in recent years, materials with antibacterial surfaces, inspired by structures found in nature, have been a point of interest for researchers. These antibiotic-free surfaces interact directly with the bacteria structure, damaging the bacteria independently of its antibiotic resistance.[4,6]

Apart from the intrinsic material properties, additional functionalization and applications may be rendered possible through the generation of laser-induced micro- and nanostructures at the surface. One simple, robust way to obtain such nanostructures is the processing of laser-induced periodic surface structures (LIPSS). LIPSS are described as grating-like structures formed upon laser irradiation on metallic, semiconducting, and dielectric surfaces.[7] These nanostructures are dependent on the laser beam polarization and wavelength and appear under a wide range of pulse durations.[8,9] This technology offers the possibility of controlling the nanostructure morphology and enabling the processing of large surface areas in a single step. Usually, the ratio between the LIPSS spatial period and the laser irradiation wavelength allows us to distinguish between so-called high and low spatial frequency LIPSS (HSFL and LSFL, respectively). For normal incidence radiation, LSFL typically exhibit periods

L. Porta-Velilla, E. Martínez, A. Frechilla, M. Castro, G. F. de la Fuente, L. A. Angurel
Instituto de Nanociencia y Materiales de Aragón
INMA (CSIC-Universidad de Zaragoza)
C/ María de Luna 3, Zaragoza 50018, Spain
E-mail: angurel@unizar.es
J. Bonse
Bundesanstalt für Materialforschung und -prüfung (BAM)
Unter den Eichen 87, 12205 Berlin, Germany

The ORCID identification number(s) for the author(s) of this article can be found under https://doi.org/10.1002/lpor.202300589

close to the laser wavelength ($\lambda \geq \Lambda \geq \lambda/2$), while HSFL feature significantly smaller sub-wavelength periods ($\Lambda \ll \lambda/2$). Within the class of LSFL and depending on the irradiated material, ripples can be oriented either perpendicular (type LSFL-I) or parallel (type LSFL-II) to the local laser beam polarization direction.[8,10]

In the case of metallic surfaces, ripples (LSFL-I) are mainly oriented perpendicular to the linear beam polarization axis.[8] This type of ripple is caused by scattering and interference of the incident radiation with a surface electromagnetic wave (SEW) generated at the rough surface.[10] The spatial period of the ripples depends on the laser wavelength (λ), the laser polarization, and the angle of incidence (θ), defined as the angle between the laser beam direction and the normal to the surface.[11–16] In the case of p-polarization (i.e., when the electric vector of the incident light is in the plane of incidence) ripples can appear with two characteristic periods, $\Lambda^{\pm}(p)$, which consider the excitation and propagation of surface electromagnetic magnetic waves (SEW), e.g. Surface Plasmon Polaritons (SPPs)[13,14]:

$$\Lambda^{\pm}(p) = \frac{\lambda}{Re(\eta) \mp \sin\theta} \tag{1}$$

$Re(\eta)$ is the real part of the effective refractive index of the air-metal boundary, $\eta = (\epsilon_{air}\epsilon/(\epsilon_{air}+\epsilon))^{1/2}$, where ϵ_{air} and ϵ are the dielectric constants of air and metal, respectively. The complex-valued dielectric permittivity ϵ is given by $\epsilon = (n^2-k^2) + i(2nk)$, where n and k are the real and imaginary parts of the complex refractive index of the metal at the laser wavelength. Note that in this equation, for non-normal incidence ($\theta \neq 0$), the Λ^+-branch relates to the minus-sign on the right-hand-side and refers to supra-wavelength LIPSS, while the Λ^- refers to the plus-sign and refers to sub-wavelength LIPSS. This intended definition may differ from other references here.

For s-polarization (i.e., when the electric vector of the incident radiation is perpendicular to the plane of incidence) the most pronounced ripples will have a period given by[13]:

$$\Lambda(s) = \frac{\lambda}{\sqrt{Re^2(\eta) - sin^2\theta}} \tag{2}$$

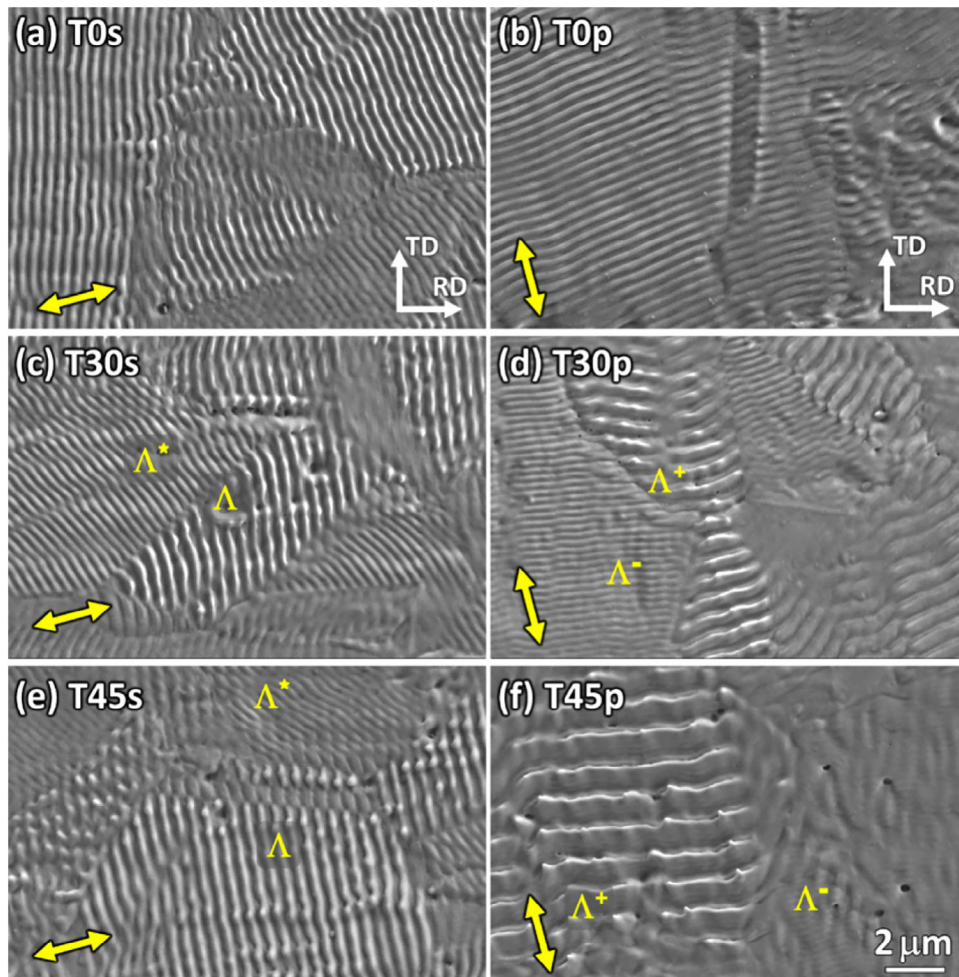This phenomenology has been experimentally observed on many metals, such as Pt, W, Ni, or steel.[17,18]

In a previous work,[19] it was found that the laser-induced nanostructures formed on a nickel alloy surface upon irradiation with a 300-ps ultraviolet (UV) laser were strongly dependent on the crystallographic grain orientation. In particular, this behavior was observed on a biaxially textured nickel alloy tape using a broad range of laser fluence values, and contrasts with typical LIPSS generated with fs-lasers. Despite the very low crystal misorientation angles in those analyzed tapes, six different nanostructures were distinguished. In this Ni alloy, the influence of the sample rolling direction and the asymmetrical distribution of the nanostructures over the surface grains, depending on their crystallographic orientation, were also first described.

On the other hand, from the processing point of view, it is also important to develop laser scanning protocols that can be scaled to process large surface areas. One approach is to use the Laser Line Scanning (LLS) methodology,[19–21] where the focused laser beam repeatedly describes a line in a given direction, while the sample moves continuously in the perpendicular one. The control of beam overlapping in the direction of laser beam scanning is performed by adjusting the repetition frequency and the laser scanning velocity. In addition, the overlap in the perpendicular direction can be controlled by adjusting the laser scan line length and the sample displacement velocity. This technology can be used to process long samples in a uniform way — in contrast to the standard Laser Beam Scanning (LBS) configuration, where the laser beam scans the surface —normally following either a meander or equally spaced lines— without moving the sample. The homogeneity of the LBS treatment may be limited by the variations in the incidence angle during the laser treatment. Also, the maximum area that can be treated homogeneously is limited by the scan field associated with the focussing lens.

Several works have observed that grains with different crystallographic orientations present different nanostructures after irradiation.[16,19,22–24] These works cover a wide range of pulse durations, laser wavelengths and materials: a 6 ns, 532 nm laser creating LSFL-I on AISI 304 austenitic stainless steel and (100) polished silicon surfaces,[16] a 300 ps, 355 nm laser creating hexagonally-arranged nanopillars on Ni-W alloy,[19] a 240 fs, 800 nm laser creating HSFL on X10NiCrAlTi alloy and AISI 316 stainless steel,[22] a 50 fs, 800 nm laser creating LSFL-I on polycrystalline nickel,[23] or a 200 fs, 1020 nm laser creating HSFL on AISI 301 stainless steel.[24] Generally, the experimental conditions where such a correlation with the material's grain structure is observed are more relevant when nanosecond or picosecond laser pulses are used to generate LSFL-I or hexagonally-arranged nanopillars. By contrast, when femtosecond lasers are used, this correlation is observed only for HSFL, or when LSFL-I are starting to emerge (i.e., at fluences closely above their formation threshold and a relatively low number of laser pulses) and it is lost again once the generated nanostructures (HSFL or LSFL) self-organize across the entire polycrystalline surface. To explain these effects it was suggested that the coupling of the optical radiation to the material, its damage threshold, and the conditions for reaching complete surface melting may vary with the individual grain orientations.[22,23] Moreover, Nürnberger et al.[16] pointed out that the grain boundaries may limit the propagation of laser-induced SPPs, thus, confining some inter- and intra-pulse feedback effects to individual grains during the LIPSS formation.

In this work, LLS using a 300 ps UV laser has been applied on rolled stainless steel (AISI 316L) surfaces in order to identify the different nanostructures that can be generated on this material. The effect of the crystallographic grain orientation on the generated nanostructure characteristics was systematically analyzed. Moreover, different processing strategies - including the relation between the laser beam scanning and the polarization directions, and the angle between the laser beam and the sample surface - were experimentally investigated. The objective is to analyze their effect on the homogeneity of the resulting nanostructured surface covered mainly by LSFL-I and to identify extended approaches that can increase the areal coverage by the desired surface nanostructures.

ADVANCED
SCIENCE NEWS

www.advancedsciencenews.com

LASER
& PHOTONICS
REVIEWS

www.lpr-journal.org

Figure 1. Top-view SEM micrographs (SE) of the surface samples after different laser treatments (indicated in each image). The same magnification was used for all micrographs. Sample tilt angle α was 0° in (a) and (b), 30° for (c) and (d) and 45° in (e) and (f). The yellow double arrows correspond to the projection of the polarization direction (PD) on the treated surface. Beam scan direction (BSD) and rolling direction (RD) are horizontal for all micrographs. With inclined samples, characteristic ripple patches with different periodicities are indicated (with values depending on α and the irradiation configuration, as explained in the text).

2. Results and Discussion

2.1. Characterization of the Laser-Generated Nanostructures and Their Spatial Periods

An example of the micro- and nanostructures obtained for each treatment is shown in **Figure 1**. When the sample tilt angle is zero, only one type of nanostructure is observed, which corresponds to 1D periodic structures, specifically to type LSFL-I.[8] Figure 1a,b shows two examples of these types of ripples, observed for samples with T0s and T0p treatments, respectively. Their spatial period, Λ, was estimated from these SEM images as 360 ± 20 nm, similar for both treatments (**Table 1**). As expected for metals, these types of ripples are oriented in the direction perpendicular to the laser beam polarization axis.[8,13]

SEM micrograph observations suggest that the grain boundaries are well defined after laser processing. Previous research on a Ni-W alloy[19] reported that some periodic surface structures (i.e., hexagonally-arranged nanoprotrusions) continued across grain boundaries for nearly normal incident radiation. In the present study, however, such behavior was rarely observed for grating-like nanoripples. Nevertheless, in some cases, it is possible to see the propagation of ripples over non-rippled (NR) grains, as discussed later. On the other hand, when two adjacent grains are nanostructured, in most cases the ripples cross the grain boundary.

Upon tilting the sample during the laser treatment, LSFL-I-type ripples also appeared for both polarization orientations (Figure 1c–f). Two different periodicities were observed in both cases (Table 1) and found to be dependent on the tilt angle and configuration type. Thus, for s-polarization, the ripples with larger periods (Λ) are oriented mostly perpendicularly to the polarization direction, nearly parallel to transversal direction (TD), and appear strongly pronounced. All these values were obtained by analyzing different grains and micrographs and have typical uncertainties of ± 20 nm in all cases. Note that there are also ripples with smaller spatial periods in this configuration (named Λ^*), which form higher angles with respect to the TD axis and
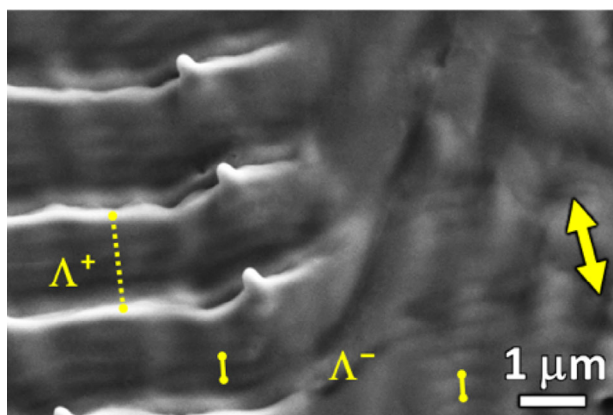
2300589 (3 of 21)

Table 1. Spatial periods of the different nanostructures obtained from the different laser treatments, measured directly on the SEM images and confirmed by 2D-FFT analysis. In the case of T0s and T0p, only one period was identified, while for tilted samples two different periods (Λ/Λ^* for s-polarization and Λ^+/Λ^- for p-polarization) were observed.

Treatment	SEM Images	2D-FFT	SEM Images	2D-FFT
	Λ [nm]		Λ^* [nm]	
T0s	360 ± 20	357 ± 5	NA	NA
T30s	440 ± 20	415 ± 10	312 ± 20	280–315
T45s	483 ± 20	494 ± 10	292 ± 20	300–360
	Λ^+ [nm]		Λ^- [nm]	
T0p	360 ± 20	357 ± 5	360 ± 20	357 ± 5
T30p	620 ± 20	650 ± 5	248 ± 20	245 ± 10
T45p	1013 ± 20	980 ± 5	219 ± 20	Nondetectable

are generally less pronounced. Most grains have one or the other type of ripples, with periods Λ being more abundant.

In the case of p-polarization, ripples with two distinct periodicities are also observed (Table 1). Note that, in this case, some grains only exhibit Λ^- ripples. When Λ^+ LIPSS are formed, however, both - Λ^+ and Λ^- - do overlap. This feature can be clearly observed in **Figure 2**, which shows a similar region to Figure 1f but with a larger magnification and enhanced contrast. Λ^- ripples appear always less pronounced, supposedly due to smaller topographic modulation amplitudes. Moreover, the ripples appear to have an inclination with respect to the normal direction of the surface for all tilted samples. This cross-sectional asymmetry increases with the angle of incidence of the laser beam with respect to the sample. As a consequence of such asymmetry, the inclination of ripples is always oriented along the direction toward the top part of the sample within the SEM micrographs (taken from the direction of the normal to the surface).

Finally, it should be mentioned that for inclined samples, there are some 2D nanostructured grains featuring a cross-hatched periodic surface pattern, although they are less abundant than the 1D-LIPSS of the LSFL-I type. Some examples of these types of nanostructures are presented in **Figure 3**, corresponding to treat-
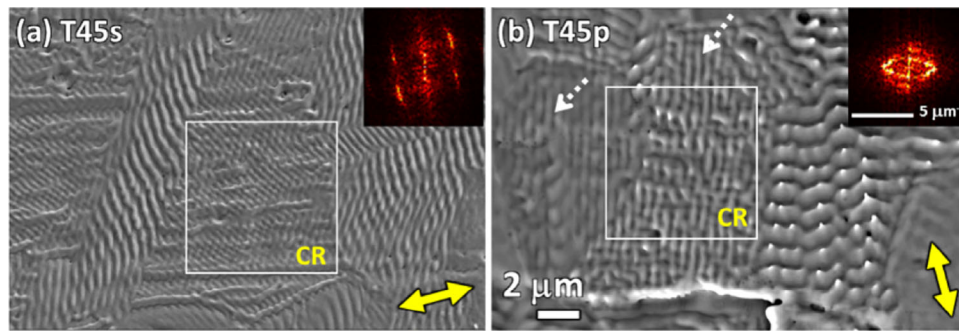
ments T45s and T45p. These nanostructures feature twinned or crossed ripples and will be named here as CR. For s-polarization, these appear as two superimposed (crossing) sets of 1D ripples that are forming a rhomboid-like structure (Figure 3a), whereas for p-polarization they exhibit a square-like structure (Figure 3b). The 2D-FFT maps of the white square highlighted zones in the micrographs are displayed in the insets. Note that on the T45p surface, there are also some grains with just ripples oriented nearly parallel to the PD (pointed by dotted arrows in Figure 3b). This will be discussed later in Section 2.2.

As shown in **Figure 4**, many grains exhibit ripples after the laser treatment (labeled "1" in the figure), although some of them are weakly visible (labeled "2"), while others appear as deformed ripples (labeled "3"). The latter are frequently present together with localized crater-shaped features and will be hereafter named "overtreated" grains (Ov). There are also some grains with "no ripples" (NR), indicated as "4" in the figure, which may either exhibit a degree of considerable roughness or very smooth surfaces. Propagation of ripples generated on adjacent grains is thus observed over some areas of the flat-surface of the NR grains in this micrograph. These may be considered general features and are observed in all sample's tilt and polarization configurations herein studied. The size of the grains does not appear to influence the generated nanostructures.

The spatial periods and the preferred orientations of the laser-generated nanostructures can be visualized by applying a Fourier analysis to the SEM images. **Figure 5** shows the 2D-FFT maps derived for both polarization configurations and at the three sample tilt angles, obtained from SEM images with a 1500× nominal magnification. The number of grains involved in this analysis is higher than in the direct measurement using FESEM images. The spatial periods obtained from these analyses are also included in Table 1. 2D-FFT patterns were obtained at distinct zones of each sample without detecting significant differences among them. Thus, the observed features in Figure 5 can be considered as reliably representative of the overall sample. In all cases, there are some bright areas at the center of the 2D-FFT maps, representing large-scale surface roughness without periodic signatures. Among all analyzed cases, these areas are less abundant in the sample with treatment T30s.

For samples T0s and T0p, LSFL-I with the same periods were formed in both polarization configurations. For $\alpha = 0°$ the LIPSS's grating vectors for samples with treatments T0p and T0s are similar, but perpendicular to each other as are the s- and p-polarization axes when considering a joint coordinate system imposed by the sample orientation. The spatial periods obtained from the 2D-FFT maps were $\Lambda(T0s) = \Lambda(T0p) = 357 \pm 5$ nm (Table 1). It can also be observed that the orientation of the lines joining the points of maximum intensity in the 2D-FFT maps is tilted $\approx 15°$ from the horizontal and vertical image directions of Figure 5a,b, respectively, consistent with the above-mentioned $\approx 15°$ deviation with respect to the laser beam polarization direction.

In the case of samples processed at tilt angles of $\alpha = 30°$ and $\alpha = 45°$, different spatial periods are observed and their characteristics are very clearly observed in this representation. The brightest areas in the spatial frequency domain depend on the tilt angle and polarization, but in all cases, they lay on the circumferences of the same radius as $\alpha = 0°$ and whose centers are

Figure 2. Top-view SEM (SE) micrograph of sample T45p showing with more detail the co-existence of the two kinds of ripples with distinct periods Λ^+ and Λ^-. The discontinuous and continuous lines mark the periods corresponding to both types of ripples. The double-arrow indicates the PD.
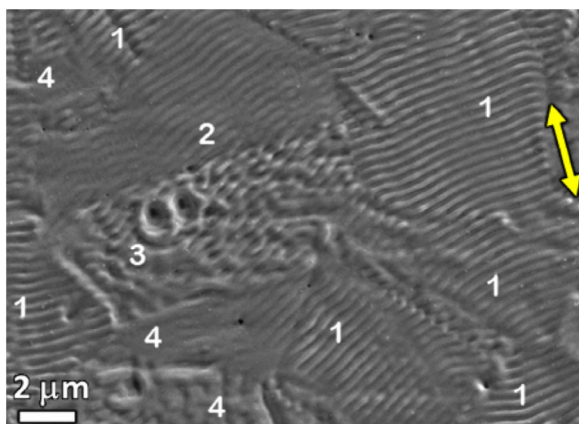
Figure 3. Top-view SEM (SE) micrographs of samples T45s and T45p showing some grains with twinned or CR ripples. The double arrows correspond to PD. The insets show the 2D-FFT maps of the white square highlighted zones in the micrographs. The same magnification was used in (a) and (b). The dotted arrows in (b) point at ripples formed nearly parallel to PD.

separated by a distance that increases with the tilted angle.[13] For s-polarization (Figure 5c,e), the brightest areas in the maps coincide with the intersection of these circles. These correspond to the Λ ripples seen in Figure 1c,e, which were aligned almost parallel to TD. The most frequent spatial periods obtained from the 2D-FFT patterns are Λ = 415 nm (T30s) and 494 nm (T45s), with typical spreads of ± 10 nm (Table 1). On the other hand, the inclined ripple patterns with reduced spatial periods Λ^*, observed in SEM images, correspond to the bright arches in the spatial frequency domain (Figure 5). Note that there exists an asymmetry between these arches (mainly in the case of T30s), so that, one of them (upper-right, lower-left) is brighter than the other (upper-left, lower-right). This is due to the misalignment between the polarization and the sample tilt angle directions. In consequence, with the characteristics of this configuration, Λ^* ripples exhibit a larger dispersion (both, in orientation and in periodicity) than Λ ripples, which are very well defined. For T30s we obtained $\Lambda^* = 280$–315 nm (more abundant with $\Lambda^* \approx 305$ nm). For T45s, the obtained values for Λ^* are typically in the range between 300–360 nm.

In the case of p-polarization (Figure 5d,f), the brighter areas in the 2D-FFT maps appear in similar arches as in the $\alpha = 0°$,

but with two well-defined periods $\Lambda^- < \Lambda(0°) < \Lambda^+$. The mean values obtained from these maps are $\Lambda^+ = 650$ nm (T30p) and 980 nm (T45p). The estimated value of Λ^- is 245 $\pm$ 10 nm for T30p. For T45p, Λ^- ripples are not visible in this representation under the magnification employed. In the case of p-polarization, there is also some dispersion in the orientation of the ripples, but the periodicity appears well defined.

The experimentally obtained ripple periods as a function of the angle of incidence are displayed in **Figure 6**. The theoretical predictions given by Equations (1) and (2) with Re(η) = 1.051 are also displayed. The Re(η) value was obtained using the optical constants of austenitic steel at $\lambda = 355$ nm ($n = 1.02$ and $k = 2.32$),[25] yielding $\epsilon = -4.32 + 4.74i$. As Re(ϵ) < -1, the steel surfaces are plasmonically active,[26] allowing a resonant coupling of the optical energy to the material's surface. In the case of p-polarization, experimental $\Lambda^\pm$ values are very similar to the predictions for p-polarization $\Lambda^\pm(p)$ based on Equation (1), with differences smaller than 5% here. In the case of s-polarization, the experimental Λ values show a rather good correspondence with the period of the strongest ripples, $\Lambda(s)$, given by Equation (2), but with experimental values systematically somewhat larger than the predictions (differences <10%).
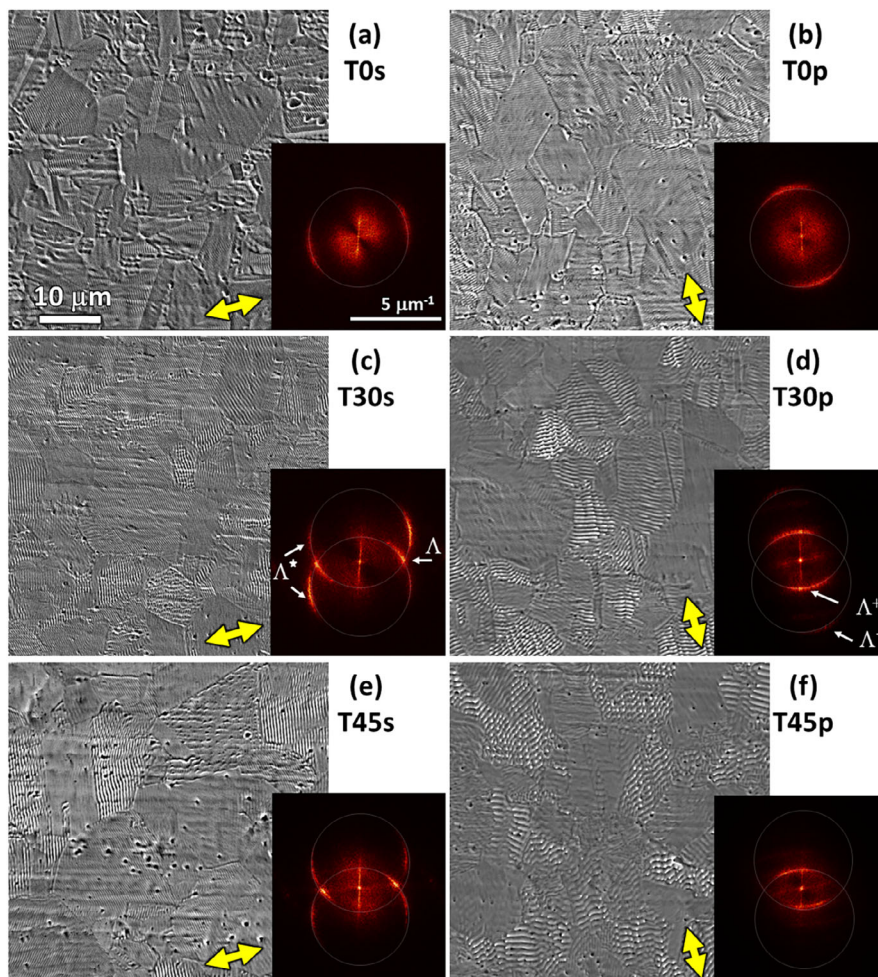

Figure 4. Top-view SEM (SE) micrograph of sample T0p showing some grains with ripples (1), weakly visible ripples (2), deformed ripples (3), which are named Ov grains. Finally, some grains (4) present no ripples (NR).

## 2.2. Theoretical Considerations: Sipe's Model of LIPSS

The SEW-model (Equations (1) and (2)) is capable of predicting spatial periods and also the figure-eight-shaped (two-crossing-circles) regions of "allowed" spatial frequencies of LIPSS, enabled by momentum conservation.[27] This model is not suitable, however, to quantify the localized energy deposition to the material that is directly related to the question, which LIPSS (type, periods, orientation, etc.) finally do manifest at the irradiated surface? For that reason, we have additionally employed here the more rigorous LIPSS theory of J.E. Sipe and co-workers,[28] which is nowadays most widely accepted, using a mathematical implementation described in detail in Ref.[[29]].

In Sipe's theory, an analytical expression of the inhomogeneous deposition of optical energy (A) absorbed at a rough surface is given via

$$A(k) \sim \eta(k) \times |b(k)| \tag{3}$$

**ADVANCED
SCIENCE NEWS**

www.advancedsciencenews.com

www.lpr-journal.org

LASER
& PHOTONICS
REVIEWS

Figure 5. a-f) 2D-FFT maps obtained from the shown SEM images of the different samples treated with different configurations, as indicated, using a nominal magnification of 1500× in all cases. The yellow double arrows indicate PD. The thin white circles on the 2D-FFT images are a guide to the eye for better visualization of the obtained spatial periods.
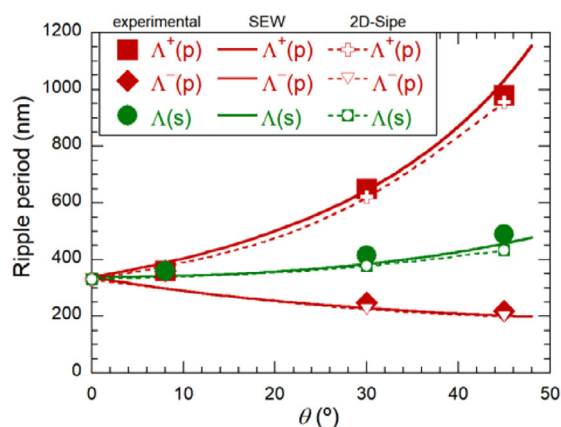
Figure 6. Spatial period values of the ripples formed at different incident angles for both configurations described in the text. Filled symbols correspond to experimentally determined values. The solid lines are theoretical predictions of the SEW-model based on Equations (1) and (2). Open symbols represent calculations based on the Sipe-theory (for details see Section 2.2) The corresponding dashed lines represent cubic spline fits to guide the eye.

where $\eta(\boldsymbol{k})$ is the so-called efficacy factor and $b(\boldsymbol{k})$ is a measure of the amplitude of the surface roughness at $\boldsymbol{k}$. The scalar function η represents the efficacy with which the surface roughness (represented by the wave vector $\boldsymbol{k}$) can absorb optical radiation in a near-surface layer, the so-called "selvedge", as the rough transitional region between the air environment and the bulk material (with a thickness $l_s \ll \lambda/(2\pi)$ and $l_s \times |\boldsymbol{k}| \ll 1$, i.e., with a thickness smaller than the laser irradiation wavelength and the spatial period Λ). The efficacy factor depends on irradiation parameters (λ, θ, PD), on material parameters (dielectric permittivity ϵ), as well on surface roughness parameters (implemented as a shape factor S and the filling factor F). Mathematically, the shape factor S represents the ratio of a lateral correlation distance l_t of the scattering centers that cover the surface to the thickness of the selvedge ($S = l_t/l_s$), while the filling factor F represents the surface fraction filled up with scattering islands.[28,31] However, it must be noted that Sipe's theory neither includes a material response (e.g., phase transitions, melt flows, chemical effects, etc.) nor any intra- or inter-pulse feedback phenomena (e.g., transient changes of optical properties, pulse-to-pulse surface topography changes, etc.).[8,30] The latter may select, and further reinforce,
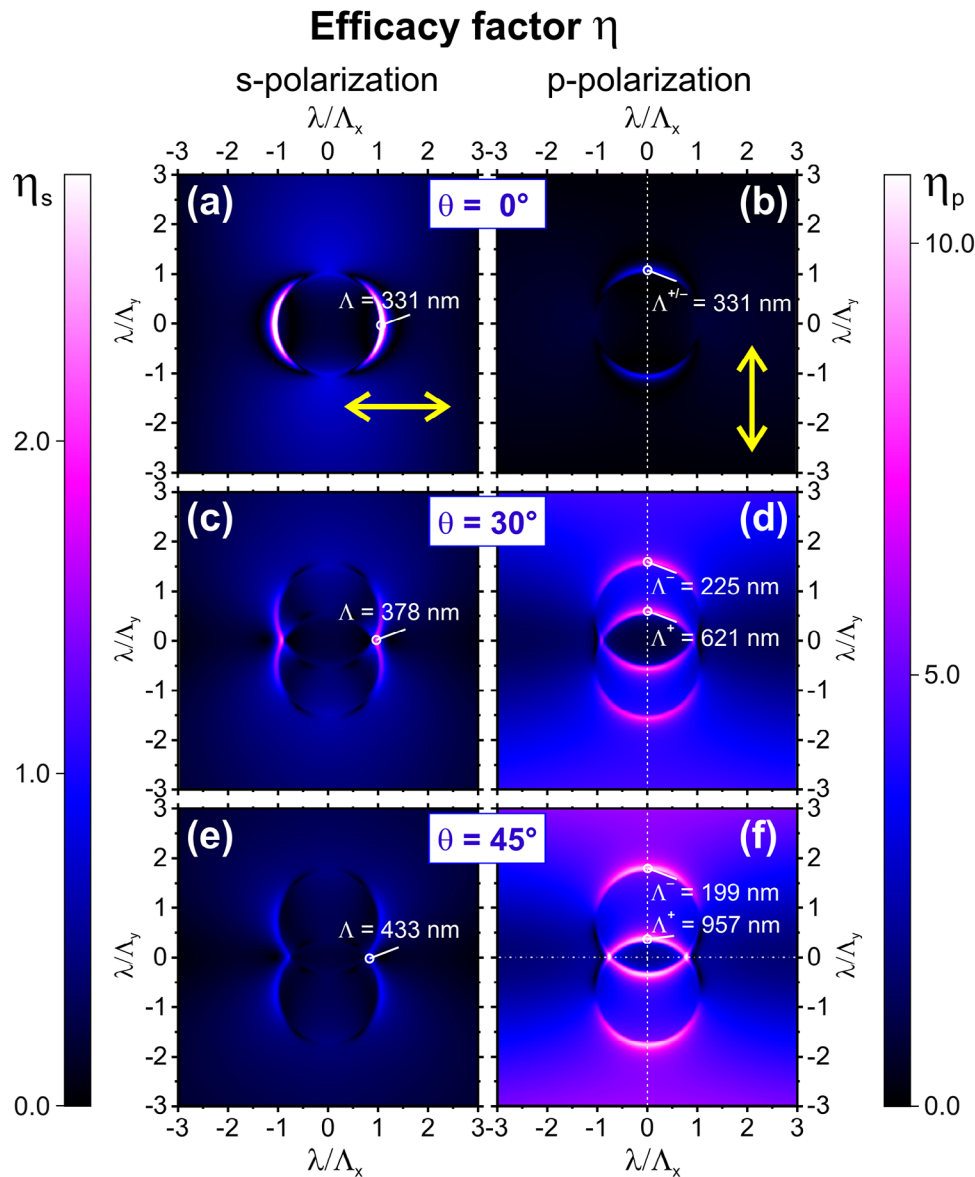
Figure 7. 2D maps of the efficacy factor η for steel as a function of the normalized LIPSS spatial frequencies ($\kappa_{x,y} = \lambda/\Lambda_{x,y}$) both ranging between ± 3. The maps for s-polarized radiation are provided in the left column, while the maps for p-polarized radiation are provided in the right column – both for angles of incidence of $\theta = 0°$ (a,b), $\theta = 30°$ (c,d), and $\theta = 45°$ (e,f), respectively. High values of η are encoded in a false-color scale with white colors. Note the different $\eta_{s,p}$ scale ranges between the columns allowing to visualize the contrary trends for increasing θ values. The dashed vertical and dash-dotted white lines mark the positions for the cross-sections presented in Figure 8.

specific LIPSS spatial frequencies that are finally manifesting at the surface of the irradiated material. The theory includes, however, SEWs and resonant surface excitation modes, such as SPPs, and can also be extended to include transient changes of the optical constants.[11]

For a non-irradiated surface, b is usually a slowly varying function with homogenously distributed spatial frequencies and without sharp peaks. Opposed to that, η can exhibit pronounced sharp peaks at specific spatial frequencies k ($k = |\mathbf{k}| = 2\pi/\Lambda$), which can be used to evaluate the associated spatial periods Λ. For that, we use normalized spatial frequencies κ, where the spatial period and the irradiation wavelength are related via $\kappa = \lambda/\Lambda$.

Figure 7 assembles Sipe-model calculations of the efficacy factor η for s-polarized (left column) and for p-polarized UV (355 nm) radiation (right column) incident at different angles [$\theta = 0°$ (top), $30°$ (middle), and $45°$ (bottom)] to a steel surface. The normalized spatial frequencies $\kappa_{x,y} = \lambda/\Lambda_{x,y}$ range from -3 to $+3$ in both spatial directions. η is encoded in a false-color scale with white colors. Note that the η-scale range varies between the left and the right columns, as specified in their color scales presented in the left and right part of the figure. The dielectric permittivity was set to $\epsilon = -4.32 + i4.74$ (the same as for the SEW-model above) and the surface roughness of the steel surfaces was modeled using "standard roughness parameters", i.e., $S = 0.4$ and

2300589 (7 of 21)

$F = 0.1$, representing localized spherically shaped defects acting as scattering centers at the rough surface.[31] A first general observation is that for increasing θ values, the amplitudes of η_s decrease, while for η_p they increase strongly. In other words, whenever p-polarized radiation components are present at a tilted surface, they tend to control LIPSS formation.

For normal incident radiation ($\theta = 0°$), the efficacy factor is dominated by two sickle-shaped arcs. As expected, among both polarizations, the pattern is rotated by 90° and represents the classical LSFL-I structures that are formed perpendicular to the laser beam polarization (indicated by yellow double-arrows in Figure 7a,b). The calculated data are quantitatively identical (as there is no difference between s- and p-polarization for normal incidence) but appear different here through the altered colourscales used among the η_s- and η_p-columns. The sickle-shaped arcs convincingly resemble the dominant features of the experimental 2D-FFT patterns previously shown in Figure 5a,b. Differences in the orientation are caused by the somewhat rotated polarization direction in that figure. The features of the 2D-FFT patterns visible as background or central peak represent large-scale grey tone variations in the corresponding SEM images and are not relevant for the LIPSS modeling. The positions of the local η_s- and η_p-peak maxima are marked by white open circles in Figure 7a,b. From the corresponding normalized spatial frequency κ, the associated spatial period of $\Lambda = 331$ nm can be calculated.

For an angle of incidence increased to $\theta = 30°$ (Figure 7c,d), the two sickle-shaped arcs split into two arc-sets while shifting and extending in the vertical direction of the figure. For s-polarized radiation (Figure 7c), the two maxima of η_s are located on the axis $\kappa_y = 0$, where the two arcs intersect and superimpose in the positive and negative κ_x-half-spaces. For p-polarized radiation (Figure 7d), the two sets of arcs resemble an eye-shaped pattern, arranged in an upright standing configuration of two intersecting circles (as predicted by momentum conservation already in the SEW model). These features were named "type-s^+ and -s^- fringes" in the original Sipe-theory.[28,31] For both cases, i.e., the s- and the p-polarized radiation, LIPSS oriented perpendicular to the polarization are predicted here by the Sipe-theory. Again, the positions of the maxima of the η-maps are marked here by circles, resulting in $\Lambda(s) = 378$ nm, $\Lambda^+(p) = 621$ nm, and $\Lambda^-(p) = 225$ nm. When comparing the calculated η_p-map shown in Figure 7d with the corresponding 2D-FFT pattern provided in Figure 5d, it becomes obvious that the inner eye-shaped peak-features of the η_p-map are strongest experimentally. This aspect will be discussed later in more detail.

At the largest angle of incidence of $\theta = 45°$ modeled in this work, the observations and trends discussed already for $\theta = 30°$ are still valid. Here, the values for $\Lambda(s) = 433$ nm, $\Lambda^+(p) = 957$ nm, and $\Lambda^-(p) = 199$ nm, were derived. With increasing θ, Λ^+ further increases, while Λ^- decreases. $\Lambda(s)$ depends less on the angle of incidence. When adding the $\Lambda(s)$, $\Lambda^+(p)$, and $\Lambda^-(p)$ values derived from the η-maps as an additional data set to Figure 6, excellent agreement is found between the SEW-model represented by Equations (1) and (2) and the Sipe-theory. Interestingly, in the η_s-map of Figure 7e, the two points of intersecting arcs localized at the abscissa ($\kappa_y = 0$) do not exhibit locally increased amplitudes anymore. All four arcs appear with similar amplitudes here. In contrast, in the η_p-map of Figure 7f, the two intersection points

of both allowed circles appear brightest and would represent very regular LIPSS oriented parallel to the beam polarization. This is fully in line with the early observations of Young et al. for elevated angles of incidence,[31] who named these features "type-c fringes".
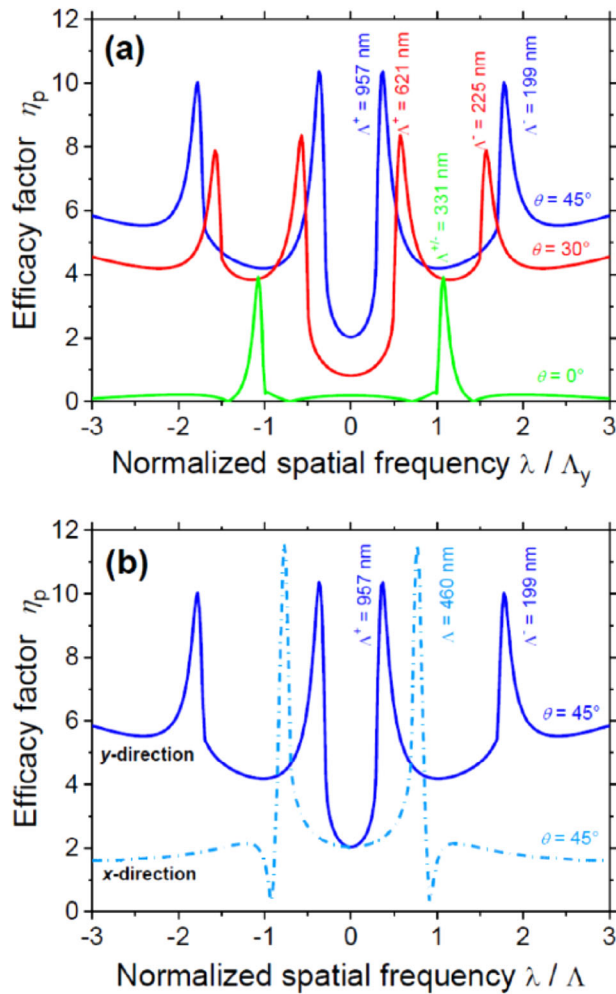
For p-polarized radiation, these "c-type fringe" structures are present on some T45p grains (discontinuous arrows in Figures 2 and 3b), and they are also an essential part of the CR ripples observed on some grains (Figure 3b and inset). In view of Sipe's theory, these CR(p) are a simultaneous manifestation of very regular cross-fringe LIPSS oriented parallel to the polarization with somewhat irregular supra-wavelength "type-s fringe" LIPSS oriented along its perpendicular. Thus, the "crossing angle" accounts to 90°. The co-existence of type-s and -c fringe structures on specific grains points toward quantitatively similar amplitudes of the efficacy factor η_p under those specific excitation conditions.

In the case of s-polarized radiation, the CR(s) ripples rather manifest, when all four sickle-shaped arcs equally contribute to the energy deposition, resulting in near-wavelength sized spatial LIPSS periods and crossing angles < 90° (depending on θ), see Figure 3a. Note that Sipes's theory will also explain the cross-ripples properties observed by Nürnberger et al.[16] on irradiated steel (AISI 304) surfaces at $\theta \geq 45°$ using a different laser (6 ns pulses and $\lambda = 532$ nm) and p-polarization.

Hence, for a quantitative comparison, cross-sections of η_p were extracted along the dashed vertical and dotted horizontal lines indicated in Figure 7 (right column) and plotted in **Figure 8**. Figure 8a compares the vertical cross-sections through the η_p maps for the three different angles of incidence θ, as depicted in Figures 7b ($\theta = 0°$), d ($\theta = 30°$), and f ($\theta = 45°$). Here, the splitting of the peak pair in the green curve for $\theta = 0°$ into a double-pair of peaks associated with the sub- and supra-wavelength LIPSS is evident when the angle of incidence increases to $\theta = 30°$ (red curve) and $\theta = 45°$ (blue curve). Note that for non-normal incidence ($\theta \neq 0°$) always the supra-wavelength peak (associated with periods Λ^+) exhibits the largest peak amplitude, i.e., the largest optical absorption at its specific spatial frequencies. Supposedly, the positive inter-pulse feedback mechanism then selects and reinforces these spatial frequencies, eventually leading to Λ^+-LIPSS dominating the rippled surface morphologies (see Figure 5, right column). Note that the background level rising with κ, particularly for increasing angles of incidence θ, does not represent a real energy deposition to the material and is caused by limitations imposed through assumptions made during the development of the theory.[28] Figure 8b compares the central horizontal (x-direction, dash-dotted line) and vertical (y-direction, solid line) cross-sections through the η_p-map calculated for $\theta = 45°$ (Figure 7f). It confirms that the peak amplitude is largest at the normalized spatial frequency $\kappa_x = \lambda/\Lambda_x \approx \pm 0.77$, representing "type-$c$ fringe" LIPSS parallel to the laser beam polarization with a spatial period ≈ 460 nm (see Figure 3b).

In summary, the calculations based on the Sipe-theory enable the interpretation of many of our experimental observations, including i) a direct correlation of the 2D-FFT's of the experimental LIPSS patterns with predictions of the spatial frequencies featuring the largest optical absorption, ii) the explanation of the predominance of "type-s fringes" LIPSS (LSFL-I) oriented perpendicular to the s- or p-polarized laser radiation, being larger for p-polarization, iii) the unveiling of the origin of the CR ripples

**ADVANCED
SCIENCE NEWS**

www.advancedsciencenews.com

**LASER
& PHOTONICS
REVIEWS**

www.lpr-journal.org

Figure 8. Efficacy factor η_p for steel as a function of the normalized LIPSS spatial frequencies ($\kappa_{x,y} = \lambda/\Lambda_{x,y}$) for three different angles of incidence ((a), along the dashed lines in Figure 7b,d,f)) and in two orthogonal directions ((b), along the dash-dotted lines in Figure 7f)).

for both laser beam polarization configurations, and iv) the observation of "type-c fringes" LIPSS for p-polarized light at large angles of incidence (T45p).

## 2.3. Influence of the Grain Orientation on the Generation of LIPSS

As mentioned above, the effect of laser processing is not homogenous over the whole rolled stainless steel surface here. Thus, it is important to analyze the grain crystallographic orientation and its influence on the specific type of surface structure generated upon laser processing. For this purpose, the method explained in Experimental section and Appendix A was used.

Figure 9 presents the RD-TD maps corresponding to samples T0s (Figure 9a) and T0p (Figure 9b) irradiated at near normal laser beam incidence. As explained in Appendix A, each point of the figure corresponds to a particular grain i on the surface, whose (RD_i, TD_i) components were obtained using the

measured Euler angles for that specific grain, Equation (A4), and mark its corresponding projection in the map. The used symbol corresponds to a specific type of observed nanostructure (i.e., overtreated, ripples, weak ripples, and no-ripples). Axes values are given in units of e, being $e = a/2$, where a is the lattice parameter. The circumferences indicate specific deviation angles with respect to the normal of the sample surface ($E2_i$). It is clear from the figures that the orientation of grains imposes the type of laser-generated nanostructures. In addition, this nanostructure is different depending on the polarization direction. Thus, in s-polarization, where PD and BSD are almost parallel (Figure 9a), grains mostly aligned with the laser polarization (direction PD of the yellow double-arrow) present ripples (Λ, Weak Λ, and Ov). Among them, grains with $E2_i > 29°$ present the most pronounced ripples, while those with (RD_i, TD_i) closer to the coordinate's origin (specifically, with $E2_i < 29°$) are identified as the most treated grains (Ov). Finally, the grains oriented perpendicular to the laser beam polarization direction present predominantly no ripples (NR).

For p-polarization, with PD almost perpendicular to BSD (Figure 9b), the strongly rippled grains (Λ) have a behavior similar to the laser treatment T0s, i.e., they also appear in this map on grains oriented around PD and with deviation angles $E2_i$ higher than 29°. Nevertheless, contrary to T0s, only grains in one of these areas around PD ($TD_i < 0$) exhibit both, the strongest ripples and the overtreated grains (the latter for $E2_i < 29°$). In contrast, in the upper part of the T0p map ($TD_i > 0$), ripples are also observed for $E2_i > 29°$, but these are mainly weakly marked (Weak Λ). Grains without ripples are predominantly observed in the upper part (half) of this map. The total percentage of rippled grains for T0s is 44% (29% for Λ and 15% for weak Λ) and for T0p it is 52% (32% for Λ and 20% for weak Λ). In the case of overtreated grains, these values are 25% for T0s and 11% for T0p, respectively.
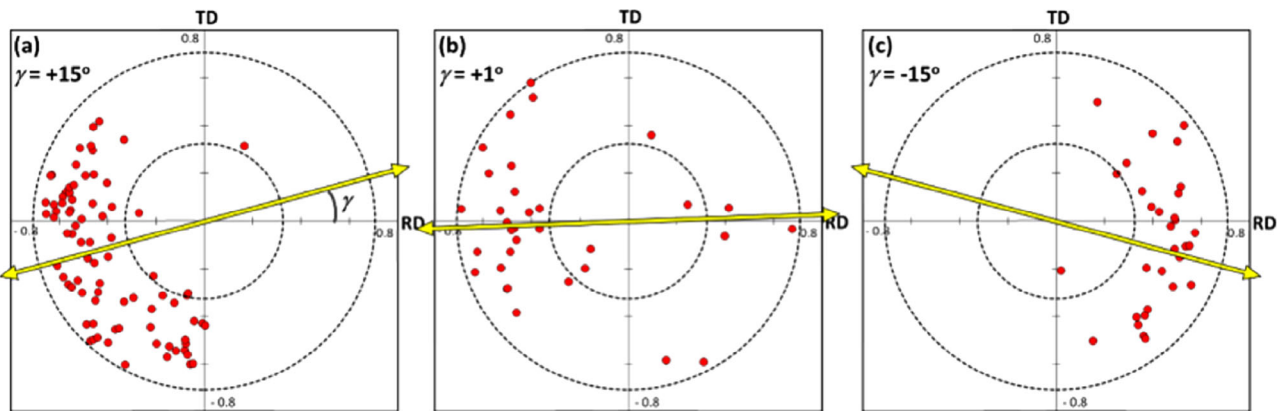
A similar grain orientation analysis was performed on a sample tilted during laser processing and the results are plotted in **Figure 10**. For s-polarization, when the angle of incidence was increased to 30° and 45° (Figure 10a,c, respectively) both overtreated and no-ripples grains are oriented in a similar fashion to the laser treatment T0s (Figure 9a). That implies that fewer ripple grains exhibit higher misorientations with respect to the normal to the surface. Hence, they appear mostly perpendicular to the laser polarization, whereas overtreated grains are located closer to the origin in the plot. As mentioned in Section 2.1, the increase in tilt angle induces two types of ripple periodicities, Λ and Λ^*. Surprisingly, these results show that, for both incidence angles, there exists a preferential grain orientation. Thus, grains oriented with $RD_i < 0$ in the RD-TD grain orientation map show mainly ripples with a period Λ, whereas the ones with an orientation associated to $RD_i > 0$ present a period Λ^*. Note that sample T30s exhibits a significant increase in the total amount of ripple-textured grains (76% overall: 49% Λ, and 27% with Λ^*). The amount of non-treated (15%) and overtreated grains (4%) was notably reduced for the latter in comparison with sample T0s. Finally, it should be noted that the nanostructured grains with crossed ripples (CR, Figure 3a), are only observed on very few grains (4%). In these cases, the visual amplitude of the ripples can be associated with the laser polarization. Thus, the grains oriented around the polarization direction present mostly
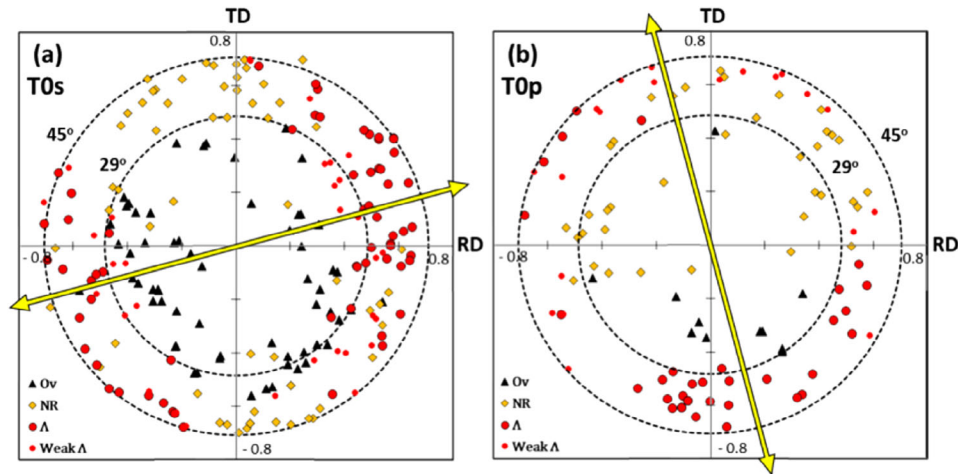
Figure 9. RD-TD grain orientation map obtained for samples irradiated at near normal incidence: a) T0s and b) T0p. Each symbol corresponds to an analyzed grain, whose (TD_i, RD_i) components have been calculated using Equation (A4). The axes values are given in units of e and the circumferences represent specific $E2_i$ angles (see **Figure A1**). The different symbols correspond to the type of nanostructures observed for each grain (see Figures 1 and 4): Ov (overtreated); NR (no-ripples); Λ (ripples); Weak Λ (weakly visible ripples). The yellow double-arrow lines represent the laser polarization direction (PD).
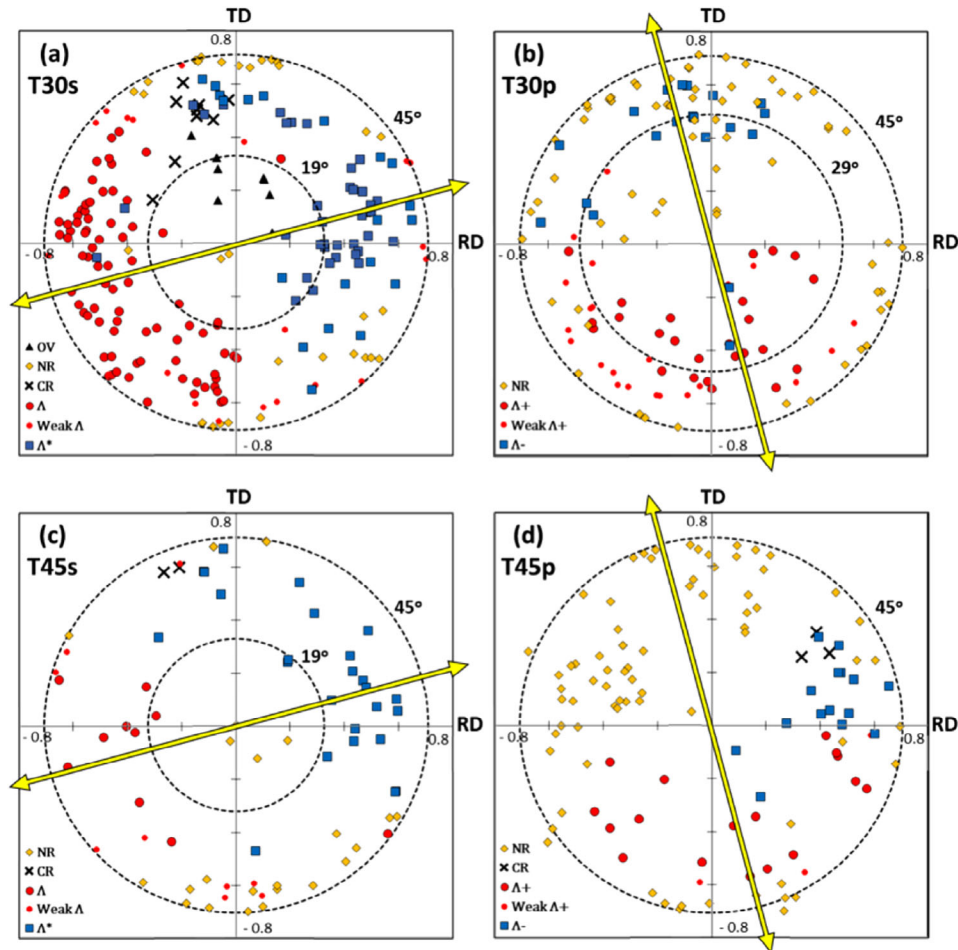
Figure 10. RD-TD grain orientation maps obtained for samples after laser treatments with the sample tilted: a) T30s, b) T30p, c) T45s, and d) T45p. Each symbol corresponds to an analyzed grain whose (TD_i, RD_i) components have been calculated using Equation (A4). The axes values are given in units of e and the circumferences correspond to fixed $E2_i$ values, as indicated (see Figure A1). The different symbols correspond to the type of nanostructure observed for each grain (see Figures 1, 3, and 4): Ov (overtreated); NR (no-ripples); Λ, Λ^*, Λ^+ or Λ^- (ripples); Weak Λ or Λ^+ (weakly visible ripples); CR (cross ripples). The yellow double-arrow lines represent the laser PD projection on the RD-TD plane.

ADVANCED
SCIENCE NEWS

www.advancedsciencenews.com

LASER
& PHOTONICS
REVIEWS

www.lpr-journal.org

Figure 11. RD-TD grain orientation maps obtained for samples after laser treatments with $\alpha = \theta = 30°$ and around s-polarization with deviation angles γ of a) $+15°$ (sample T30s), b) $+1°$, c) $-15°$. Each symbol corresponds to an analyzed grain, whose (TD_i, RD_i) components have been calculated using Equation (A4). The axes values are given in units of e and the circumferences correspond to fixed $E2_i$ values as indicated (see Figure A1). Only the grains with marked ripples of period $\Lambda(s)$ are shown (see complete maps in Figure B1). The yellow double-arrow lines represent the laser PD projection on the RD-TD plane.

well-visible ripples (both Λ and Λ^*). Qualitatively, the behavior of sample T45s is very similar to that of sample T30s.

Surfaces treated with p-polarization at $\alpha = 30°$ (T30p) just exhibited three types of grain structures: no ripples (NR) and LSFL-I structures with both, supra-wavelength (Λ^+) and sub-wavelength (Λ^-) spatial periods. The distribution of the nanostructures across the grains is similar to the one observed in treatment T0p, but in this case, ripples (Λ^+) appear on grains with $TD_i < 0$, while no ripples (NR) appear mostly on grains oriented upward ($TD_i > 0$). In the latter case, weak ripples (weak Λ^+) are present on the left side of the grain orientation map ($RD_i < 0$) with deviation angles above $\approx 29°$. Interestingly, with this configuration (T30p), it is not possible to generate ripples on grains with high deviation angles (i.e., $E2_i$ close to $45°$), independently of the grain orientation itself. It is important to highlight that almost all the grains in this sample present sub-wavelength period ripples (Λ^-). Nevertheless, most of them are only very weakly visible and cannot be distinguished without using large magnification. Thus, in this grain orientation map, only the strongly visible sub-wavelength period ripples are shown. Following the trends observed for previously described treatments, Λ^- ripples appear preferentially on grains oriented close to the polarization direction, mainly with $TD_i > 0$. With this configuration (T30p), 51% of analyzed grains remained without ripples.

Following the trend observed for samples T0p and T30p, grains in sample T45p with $TD_i < 0$ present ripples with supra-wavelength periods (Λ^+), while those oriented with $TD_i > 0$ and grains with a deviation angle $E2$ close to $45°$ exhibit no ripples (NR). By contrast, sub-wavelength period ripples (Λ^-) and CR ripples do not appear in grains oriented closely to the laser polarization direction. In this case (T45p), they appear on grains oriented perpendicularly to the PD and $RD > 0$. The total percentage of non-ripple grains is 66% here.

Due to the above-mentioned misalignment in our set-up, $\approx 15°$ with respect to s- or p-polarization, it is worth investigating the effect of this deviation on the obtained grain orientation maps. With this aim, we performed additional experiments for $\alpha = \theta = 30°$, but corrected this misalignment as much as permitted by our experimental setup. **Figure 11** shows the maps corresponding to

deviation angles $\gamma \approx +15°$, $+1°$ and $-15°$, where γ is the angle between PD and BSD = RD. Note that $\gamma = +15°$ (Figure 11a) corresponds to treatment T30s shown in Figure 10a. For clarity, only the $\Lambda(s)$ ripples are shown in this figure (see the complete maps, with corresponding 2D-FFT images, in Appendix B (**Figure B1**)). We observed an interesting behavior for this configuration. For $\gamma = +15°$ and $-15°$, the $\Lambda(s)$ ripples either appear at $RD_i < 0$ or $RD_i > 0$, respectively. On the contrary for $\gamma \approx +1°$ these are located at both sides of the polarization direction, although they are more abundant at $RD_i < 0$. This indicates that a small deviation around the s-polarization ($\gamma = 0°$) in these maps exerts a strong effect on the ripples. Furthermore, by analyzing the corresponding complete grain orientation maps (Figure B1a,e), we can see that the maps for $\gamma = +15°$ and $-15°$ are "equivalent" but with a mirrored symmetry with respect to the TD direction.

Similar analyses were performed for p-polarization, but in this case, we did not observe any significant difference. Thus, the map obtained for PD perpendicular to BSD = RD ($\gamma = +91°$, see Figure B2 in Appendix B) is essentially equal to the map of sample T30p ($\gamma = +105°$) in Figure 10b. In other words, supra-wavelength Λ^+ ripples appear predominantly on grains with $TD_i < 0$, while no ripples (NR) appear mostly on grains oriented upward ($TD_i > 0$) in both maps. As expected, the spatial period of the ripples does not vary significantly in this γ range in any case: $\Lambda(s) \approx 415–430$ nm, $\Lambda^+(p) \approx 630–660$ nm, and $\Lambda^-(p) \approx 240–245$ nm.

In summary, those results make clear that both, the sample tilt α (respectively the laser incidence angle θ) and the configuration between the polarization, the incidence plane, and the laser beam scanning directions are important parameters that directly determine the appearance and regularity of LSFL-I. For all the configurations reported herein, grains with orientations close to the polarization direction tend to form periodic nanostructures in both, the plane (T0s, T0p) and the tilted (T30s, T30p, T45s, T45p) samples. The introduction of a sample tilt ($\alpha \neq 0$), generates an asymmetry in the response of the grains. For p-polarization, grains pointing toward the lower part of the sample once inclined, present the most pronounced (visible) ripples, whose periodicity is given by $\Lambda^+(p)$. On the other hand, we observed a

strong influence of deviation angle γ around the s-polarization on the TD-RD maps, but with characteristic mirrored symmetries for $+\gamma$ and $-\gamma$ maps. This effect is not observed for p-polarization. Moreover, mainly on non-tilted samples ($\alpha = 0$), grains with small deviation angles from the sample's normal direction perceive more absorbed optical energy, subsequently leading to a grain-localized overtreatment, featuring a deformation of the ripple-like nanostructures. Grains with no-ripples are those aligned perpendicularly to PD for s-polarization, but not for p-polarization.

This correlation is not only observed with 300 ps UV pulses. Additional experiments have been performed using an 800 ps IR ($\lambda = 1064$ nm) laser and for normal incident radiation ($\alpha = 0°$ configuration). Some results are presented in Appendix C. SEM image presented in **Figure C1**a and EBSD analysis (Figure C1b) demonstrate that different nanostructures are obtained in grains with different crystallographic orientations. Figure C1c shows the RD-TD orientation map for some grains with two different nanostructures. Nanostructure type 1 corresponds to grains that exhibit well-defined ripples, with a period close to 1 μm. The map shows that these grains are concentrated in the region $RD_i < 0$. In contrast, grains that exhibit an emerging nanostructure are concentrated in $RD_i > 0$ region. It can be concluded that the main ideas extracted from the presented analysis can be extended to the behavior of this surface while irradiated with different laser sources when the laser processing parameters are adjusted to generate these nanostructures.

2.4. Effects of Combining Two Laser Treatments

As discussed before, all the above laser treatments generate nanostructures that depend on the grain orientation, leaving some grains without LIPSS. Thus, we have additionally investigated the possibility of combining two consecutive laser treatments to improve the final surface morphology with respect to the coverage with LIPSS. Specifically, we present the effect of performing this two-step processing with the T30s conditions, but changing the in-surface-plane orientation of the sample for the second laser treatment, as explained below. The results are shown in **Figures 12** and **13**. In detail, for the first laser treatment (T1) both samples exhibit the same nanostructures as previously exemplified in Figures 1c and 5c, related to grain orientation maps as presented in Figure 10a. Before the second laser treatment (T2), one of the samples was rotated by 90° clockwise (Figure 12) while the other one was rotated by 90° anticlockwise (Figure 13) with respect to ND. Finally, both samples were rotated back to the initial position for SEM and EBSD analysis at the initially selected positions.

Focussing on the most pronounced ripples formed for this configuration (i.e., those with spatial periods Λ(s) and oriented perpendicular to PD), we expect in both samples the presence of vertically orientated ripples (V, parallel to TD), formed during T1, as well as horizontally oriented (H, parallel to RD) formed during T2. For the first sample, V and H ripples are observed on many grains and are clearly visible in the corresponding 2D-FFT map (see the inset of Figure 12a). The spatial period related to the most pronounced feature in the 2D-FFT map is Λ(s) = 420 ±10 nm, in both directions, in agreement with the results listed in Table 1. In addition, some grains exhibit nanostructures where

V and H ripples have been added. This can be seen in more detail in Figure 12b, where the surface of the sample was inclined 70° for SEM observation (similarly as for the EBSD analyses) to better visualize the ripples' morphology. Unexpectedly, the presence of vertical Λ(s) ripples is scarce in the second sample (Figure 13a), which has more grains without ripples than the first sample, as is clearly observed in the 2D-FFT map (Figure 13c).

In order to understand the reason for this behavior, we have analyzed the RD-TD grain orientation maps obtained for both samples, displayed in Figures 12c and 13c. For clarity, only the Λ(s) ripples (with V, H, and V+H orientations manifesting as crossed ripples (CR)) are shown in these figures. Figures 12d and 13d display the expected maps composed from one of the T30s of Figure 10a, under the simple hypothesis that both maps corresponding to T1 and T2 can be just additively superimposed. Here, we have also displayed the Λ(s)-ripples corresponding to both treatments V(T1) and H(T2), but we have also added some of the NR points of T2 (those in the 4th quadrant in Figure 10a, i.e., with $RD > 0$ and $TD < 0$), needed for the discussion below. Interestingly, for the first sample (Figure 12), the experimental and the expected maps are quite similar, except that the absolute number of evaluated grains differs. Thus, the orientation of grains showing ripples is mostly as expected from the above obtained maps, and the grains showing V+H ripples in Figure 12c are those oriented in the conditions where the V and H data points overlap in the map Figure 12d. It is also important to point out that the mentioned NR(T2) data points do not overlap with the V(T1) ones. On the contrary, in the case of the sample with the anticlockwise rotation (Figure 13), we notice that the grains where Λ(s)-ripples were formed in the first treatment, V(T1), coincide in the map with the mentioned NR(T2) ones. When this occurs, the second treatment "erases" the V(T1) ripples.

We conclude that some of the grains labeled as NR (i.e., without ripples) would be "unaffected" by the laser, whereas others would suffer some melting process that erases or partially destroys the LIPSS generated on the initial laser treatment. In consequence, when the double treatment works, as in Figure 12, this process is useful to increase the number of grains with LIPSS, also generating different ripple-orientation configurations.

The observations for the two-step processing reported in this section point toward a scenario, where the grains labeled as NR exhibit a different melt and solidification dynamics than the other neighboured grains on which finally specific ripples do manifest. A further inspection and in-depth characterization of these particular grains will be required to clarify the precise material composition and structure of NR-labeled grains, which is out of the scope of this work.

3. Conclusion

The formation of LIPSS on rolled AISI 316L stainless steel surfaces was studied employing UV sub-ns laser pulses in a large area laser scanning configuration at varying angles of incidence ($\theta = 0°$, 30°, and 45°) and with different linear polarization states (s, p). At normal incidence, so-called low spatial frequency LIPSS (type LSFL-I) are the dominant surface morphology featuring spatial periods Λ around the irradiation wavelength ($\lambda = 355$ nm), while not covering all grains of the material homogeneously. For non-normal incident radiation, quasi-periodic 1D line gratings
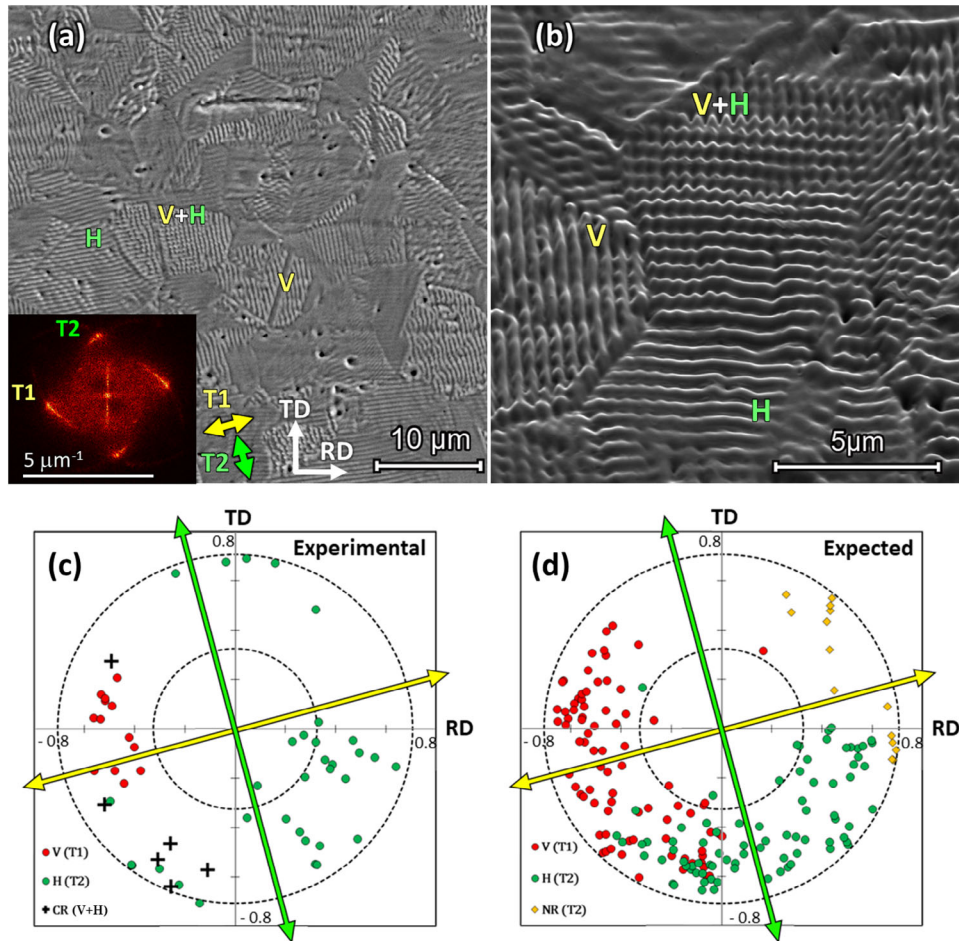
Figure 12. Results obtained for a sample after two-step laser treatment (T1+T2), using T30s conditions, with sample rotation of 90° clockwise for T2, as explained in the text. a) Top-view SEM micrograph (SE) and corresponding 2D-FFT in the inset. An example of each $\Lambda(s)$ ripple's orientation, V, H, and V+H (CR), is indicated in the SEM image. b) Detail of the ripple topography seen with the observation angle to inclined 70° (SE). c) RD-TD grain orientation map obtained experimentally for this sample. Each symbol corresponds to an analyzed grain, whose (TD_i, RD_i) components have been calculated using Equation (A4). The axes values are given in units of e and the circumferences correspond to fixed $E2_i$ values as indicated (see Figure A1). Only the grains with pronounced ripples of the period $\Lambda(s)$ are shown. The yellow and green double-arrow lines represent the laser PD projection on the RD-TD plane for T1 and T2, respectively. d) Expected RD-TD grain orientation map obtained assuming that both maps corresponding to T1 and T2 can be just additively superimposed.

of typically both supra- and sub-wavelength spatial periods manifest as LIPSS patterns in directions parallel or perpendicular to the beam polarization, or in cross-hatched surface topography patterns. A first-principle electromagnetic model (Sipe theory of LIPSS) allowed to classify the plethora of distinct surface nanostructures observed on different grains of polycrystalline steel and to explain their spatial periods as well as their sensitivity to p-polarized radiation. A practical methodology was developed to analyze the relevance of the materials (poly)crystalline grain structure on LIPSS formation: EBSD was used to construct "grain orientation maps" of the LIPSS by ordering the surface morphologies via the Euler angles of the underlying grains and a projection into Cartesian coordinates, pinpointing the importance of the materials grain crystallographic orientation for our irradiation conditions. These maps reveal that the 300 ps UV laser pulse treatment is strongly affected by the crystallographic orientation of each steel grain and may result in individually different topographic surface nanostructures. The angle of incidence of the laser radiation and the polarization direction are both crucial parameters. In our experiments, at $\theta = 30°$ the highest number of grains covered by LIPSS was observed. This behavior has also been observed when other sub-ns laser sources are used. In consequence, the conclusions derived in this work can be extended to a broad range of laser treatments.

In addition, the understanding of the observed phenomena opens the possibility of designing combinations of laser treatments with the objective of generating additive effects where the number of grains with well-defined nanostructures generated increases, thus optimizing the total areal coverage.

4. Experimental Section

Material: The experiments were performed on commercial, rolled SS316L samples provided by ACERINOX Europa (www.acerinox.com). The analyzed 0.5 mm-thick sheets were pieces of 40×40 mm^2 or 20×20 mm^2 cut from the same coil. The chemical composition of the employed SS316L
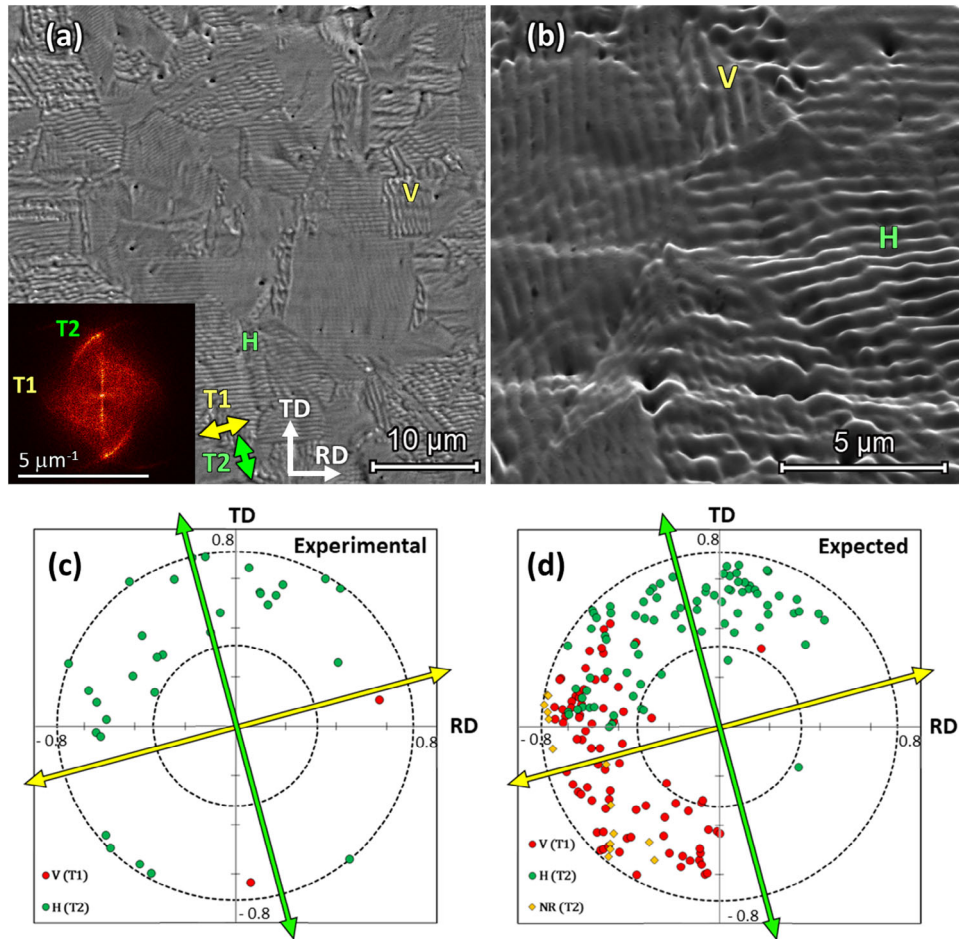
Figure 13. a-d) Similar results as in Figure 12 for the sample after two-step laser treatment (T1+T2), using T30s conditions, except that this sample was rotated 90° anticlockwise for T2 laser treatment.

material was provided by the supplier and is collected in **Table 2**. The surface had a Bright Annealed finish (or BA finish, according to the ASTM 480/480M-22 Standard), consisting of cold rolled, annealed, pickled, and skin-passed material steps. This yields a bright and reflective surface with average surface roughness (Ra) in the range between 50 and 100 nm.

Laser Processing: Surface treatments were performed using a UV pulsed laser (Rofin-Sinar, Germany) with a wavelength $\lambda = 355$ nm and a pulse duration $\tau_p = 300$ ps. The laser has a maximum output power of 2.3 W and is linearly polarized. Using a lens with a focal length of 160 mm, at the working distance the beam has an elliptical Gaussian profile with $1/e^2$ intensity decay dimensions[32] of $2a = 34$ μm and main axis ratio of $b/a = 0.86$.

As mentioned before, all treatments were performed using an LLS configuration,[19–21] schematically shown in **Figure 14**. In this work, the laser was operated at a pulse repetition frequency $f_{rep} = 300$ kHz, with an individual pulse energy $E_{pulse} = 2.08$ μJ, an average pulse fluence $F_{av} = 0.27$ J cm^{-2}, and an irradiance $I = 0.89$ GW cm^{-2}. The laser beam scanned a line with a length $l_L = 25$ mm using a velocity $v_L = 1500$ mm s^{-1}, always within the same direction. Thus, the distance between the centers of two consecutive laser pulses in a line was $\delta_{pulses} = v_L/f_{rep} = 5$ μm. Meanwhile, the sample moved in the transversal direction at a velocity $v_S = 0.132$ mm s^{-1}, resulting in a distance between two consecutive scanning lines $\delta_{lines} \approx 3$ μm. Since these values are much lower than the corresponding beam size, the accumulated energy distribution on the surface is uniform, with 1D- and 2D-accumulated average fluence values, $<F_{1D}> = 1.23$ J cm^{-2} and $<F_{2D}> = 13.89$ J cm^{-2}. These values have been obtained using a previously described procedure.[19] The above values were the same in all treatments and were selected in order to maximize the visual iridescence level generated on the sample surface as a straightforward indicator for having created pronounced LSFL-I topographies.

Different aspects relating to the processing conditions were investigated in this study (see Figure 14 and **Table 3**):

Table 2. Chemical composition (wt.%) of the analyzed SS316L samples.

Element	wt.%	Element	wt%	Element	wt.%
C	0.019	P	0.027	Ti	0.010
Si	0.35	S	0.002	Al	0.003
Mn	1.30	N	0.042	As	0.008
Cr	16.6	Pb	0.001	Co	0.13
Ni	10.0	Sn	0.007	Nb	0.013
Mo	2.06	Cu	0.31	Fe	69.1

i. A coordinate system has been defined in the sample surface by determining the rolling direction (RD), the transverse direction (TD), and the normal to the surface (ND). Laser scanning has been applied in all the cases parallel to RD.

2300589 (14 of 21)
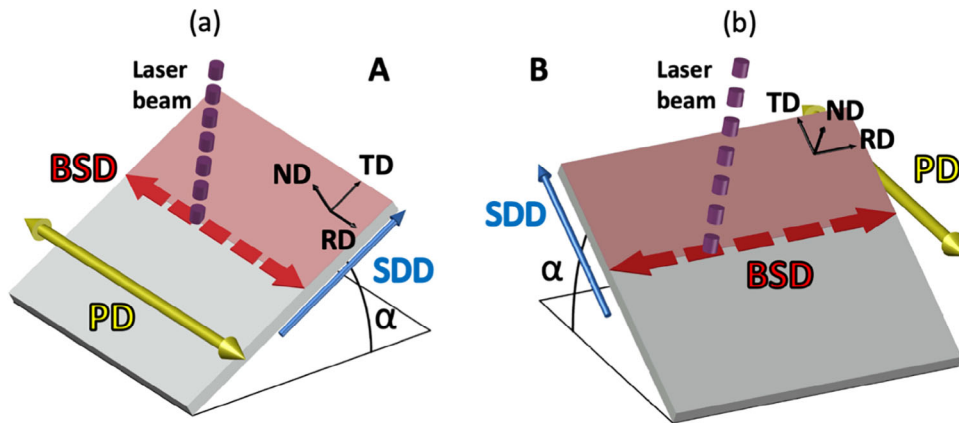
Figure 14. Scheme of the LLS processing configurations used in this work. The sample is tilted at an angle $\alpha = 0°$, 30° or 45°. The laser beam scanning direction (BSD, discontinuous red double arrow) and the laser polarization direction (PD, yellow double arrow) are nearly parallel (a) or nearly perpendicular (b). The sample displacement direction (SDD) is represented by a blue single arrow. The red rectangle is the region already treated at this specific time. The sample material intrinsic rolling (RD) and transverse direction (TD) are indicated on the sample surface, as well as the normal direction (ND), as separate Cartesian coordinate systems (black arrows).

Table 3. Set-up conditions of the performed laser treatments (see Figure 14).

Treatment	Orientation between BSD and PD	Polarization	Sample tilt angle α [°]	Incidence angle θ [°]
T0s	Near parallel	s	0	8
T0p	Near perpendicular	p	0	8
T30s	Near parallel	s	30	30
T30p	Near perpendicular	p	30	30
T45s	Near parallel	s	45	45
T45p	Near perpendicular	p	45	45

ii. The laser beam scan direction (BSD) and the polarization direction (PD) are nearly parallel (Figure 14a), or nearly perpendicular (Figure 14b). Note that in both cases, the sample displacement direction (SDD) is perpendicular to BSD.

iii. The sample tilt angle, α, which was set to 0°, 30° or 45°. The local incidence angle between the laser beam and the normal, θ, was set to 8° for $\alpha = 0°$, in order to minimize the back-reflections toward the laser system. In the other two cases, $\theta = \alpha$.

There is a small change in the incidence angle along the beam scan line. This variation is smaller than 3.3° and has been considered negligible. In Figure 14a, PD is perpendicular to the plane of incidence (s-polarization) and parallel to RD, regardless of the tilt angle. By contrast, in Figure 14b, PD is in the plane of incidence (p-polarization) and has components in TD and ND directions. As the laser treatment in the air can oxidize the material's surface[33] and consequently modify some of its properties, such as radiation absorption or corrosion behavior, all laser treatments were performed in an argon atmosphere. As it will be shown later, a careful analysis of ripple orientations of all irradiated surfaces indicated that PD was not exactly parallel or perpendicular to BSD. There was an experimental misorientation of ≈15°.

Microstructure Characterization: The surface morphology was analyzed with field-emission scanning electron microscopy (FESEM, MERLIN Carl Zeiss Oberkochen, Germany and HITACHI SU5000, Tokyo, Japan) using secondary electron (SE) detection and electron beam acceleration voltages of 5 kV. Electron Back Scattering Diffraction (EBSD) experiments were performed with the same microscope using an AztecHKL system from Oxford Instruments (Abingdon, UK) to analyze the surface crystallography.
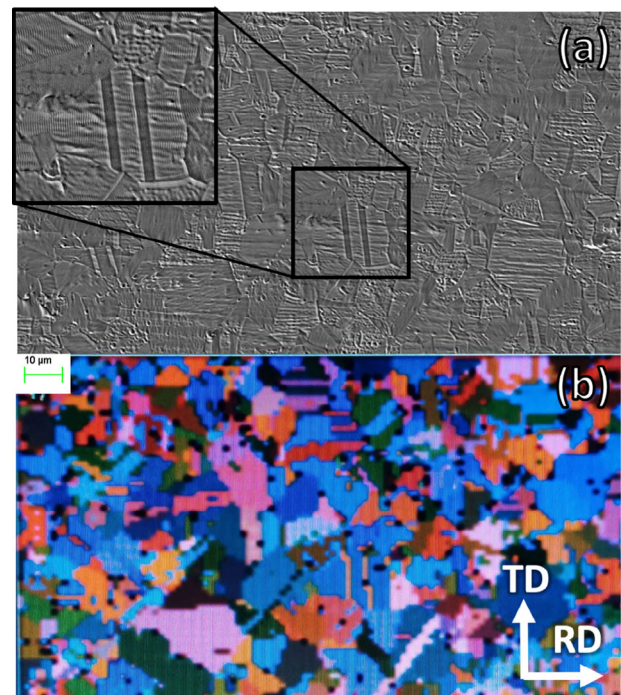
Figure 15. a) Top-view SEM micrograph (SE) of a laser-treated SS316L surface using treatment T0s showing different generated nanostructures. The inset shows the area highlighted by a square with a higher magnification. b) EBSD Euler map of the same area. Note that the same magnification was used in (a) and (b), but in the latter, the sample had to be tilted at 70° (rotated around the RD direction) explaining the reduction in grain dimensions along the vertical image direction.

2D Fast Fourier Transform (2D-FFT) maps were obtained from SEM images using the Gwyddion software (Version 2.60).

In order to correlate the laser-generated nanostructures on each grain with its individual crystallographic orientation, a systematic EBSD analysis was performed, following the procedure described in Appendix A. Initially, a general image of the interest area was taken at a nominal magnification of 700× (see **Figure 15a**). Selected characteristic grain structures were

characterized at a higher magnification (1500×). Subsequently, the sample was tilted at 70° and the EBSD analysis was performed on the same area (700×, Figure 15b) using a pixel size of $1.5 \times 1.5 \ \mu m^2$. The assigned crystallographic structure for the steel was Fe FCC, i.e., iron face-centered cubic. This map allows obtaining the Euler angles ($E1_i$, $E2_i$, $E3_i$) for each grain i. At least 100 grains were analyzed for each laser treatment.

Appendix A

In order to quantify the crystallographic orientation of each individual grain, a coordinate system has been defined. Taking into account that all the studied samples are plates or tapes obtained by rolling, the selected reference coordinate system is defined by the rolling direction (RD), the transversal direction (TD), and the normal direction (ND). A cube is associated to each grain with the orientation given by the crystallographic orientation of the grain. The origin of coordinates associated with RD, TD, and ND is placed at the center of the cube. In Figure A1a, a scheme describing this coordinate system is presented. The cube edge has a value of $a = 2e$, where a is the crystallographic lattice parameter. We monitor the position of the center of the upper side of the cube (Figure A1b) representing each grain from the measured Euler angles as explained below.
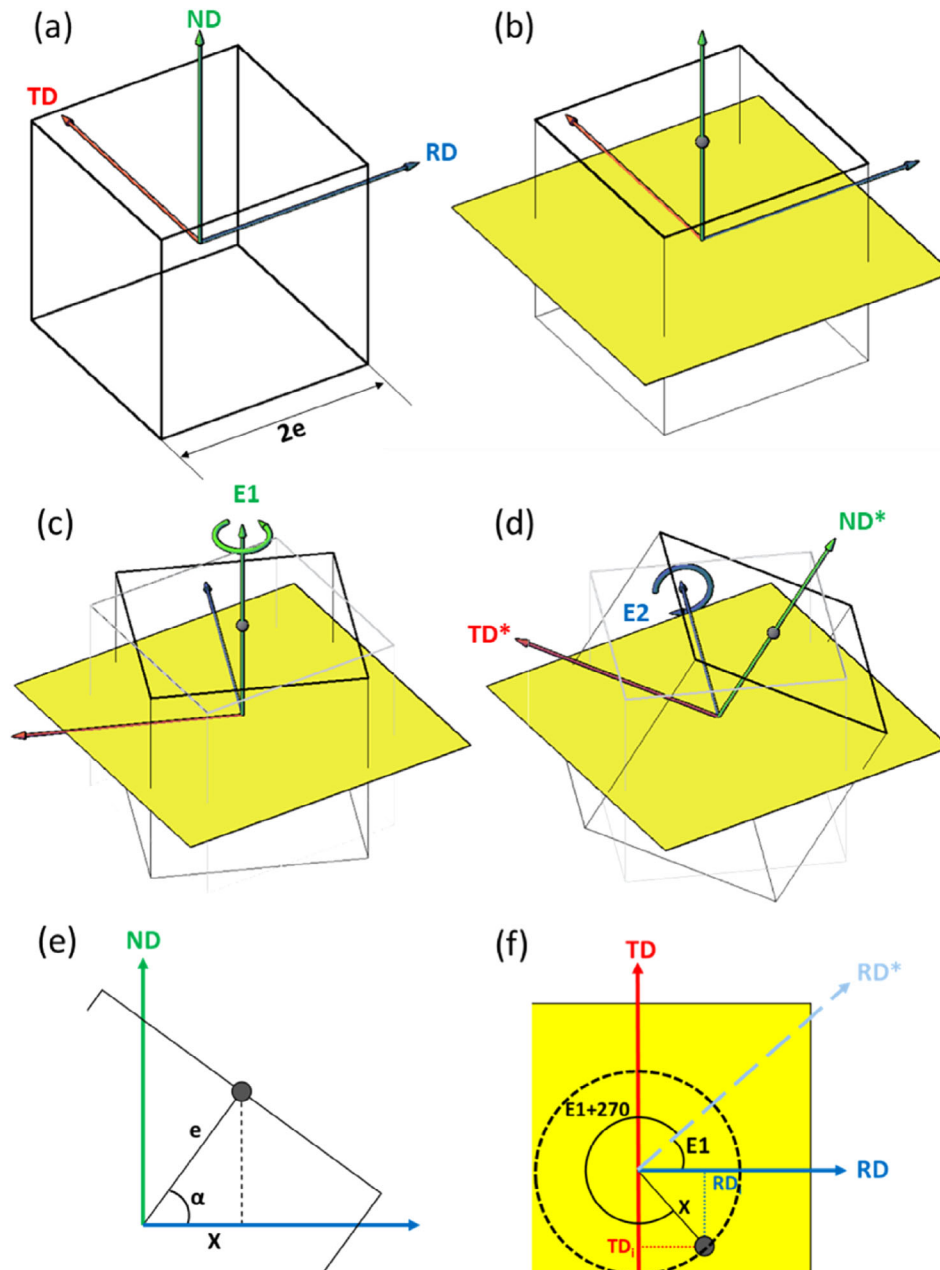
Figure A1. Representation of the analysis cube in the original position. a) The coordinates origin is located in the cube center and the three local axes coincide with the global ones (RD, TD, ND). b) The top face (black highlighted) center, represented by a black point and the RD-TD plane (yellow plane). Example of a cube position after applying the Euler rotations $E1$ (c) and, subsequently, $E2$ (d). Translation of the Euler angles $E1_i$ (e) and $E2_i$ (f). At the end of the process, the projection of the center of the upper side in the plane RD-TD (yellow square) is defined by the coordinates RD_i and TD_i. The dashed circle represents all the grains with the same $E2$ value.

2300589 (16 of 21)

Euler angles provide information on the crystallographic orientation in the surface of each grain, considering the previously described coordinate system. In order to get the actual orientation of a particular grain, a cube, initially oriented with the (RD, TD, ND) coordinate system must be reoriented following three rotations:

- The first rotation is by and angle $E1$ around the ND axis. $E1$ rotation is anticlockwise (Figure A1c).
- The second rotation is by an angle $E2$ ($0 < E2 < \pi$) around the new RD* direction. It is also anticlockwise (Figure A1d).
- The third rotation is by an angle $E3$ around the new ND* direction.

The EBSD software defines the Euler angles with the lowest $E2$ value possible. In consequence, the top face of the cube in its origin position (Figure A1a) is always the top face after the rotations. A particular crystallographic orientation will be defined by the projection of the upper side center over the original RD-TD plane after a specific rotation. The chosen reference point of the 3D position of each grain is contained in the ND* axis. In consequence, the last rotation, $E3$, does not change its final position in this 2D-Cartesian representation, and only the rotations associated with $E1$ and $E2$ have to be considered.

Considering a particular grain, with a given orientation defined by the Euler angle values: $E1_i$, $E2_i$, $E3_i$. Figure A1e shows the estimation of X, which is the distance from the projection of the reference point on the RD-TD plane to the coordinate origin:

$$X = \cos(\alpha) * e \tag{A1}$$

α is the angle between the RD* direction and the RD-TD plane. As $E2_i$ defines de deviation from the ND axis, α is defined as a complementary angle ($\alpha = 90 - E2_i$). If the cube-plane system is observed from the top (Figure A1f), $E1$ determines the angle between RD* and RD. After $E1_i$ rotation, it is important to highlight that $E2_i$ is an anticlockwise rotation so that the reference point (center of the upper side) is always placed in the perpendicular direction to the RD* axis (270°). The coordinates of the reference projected point in the RD-TD plane, RD_i and TD_i, can be estimated as:

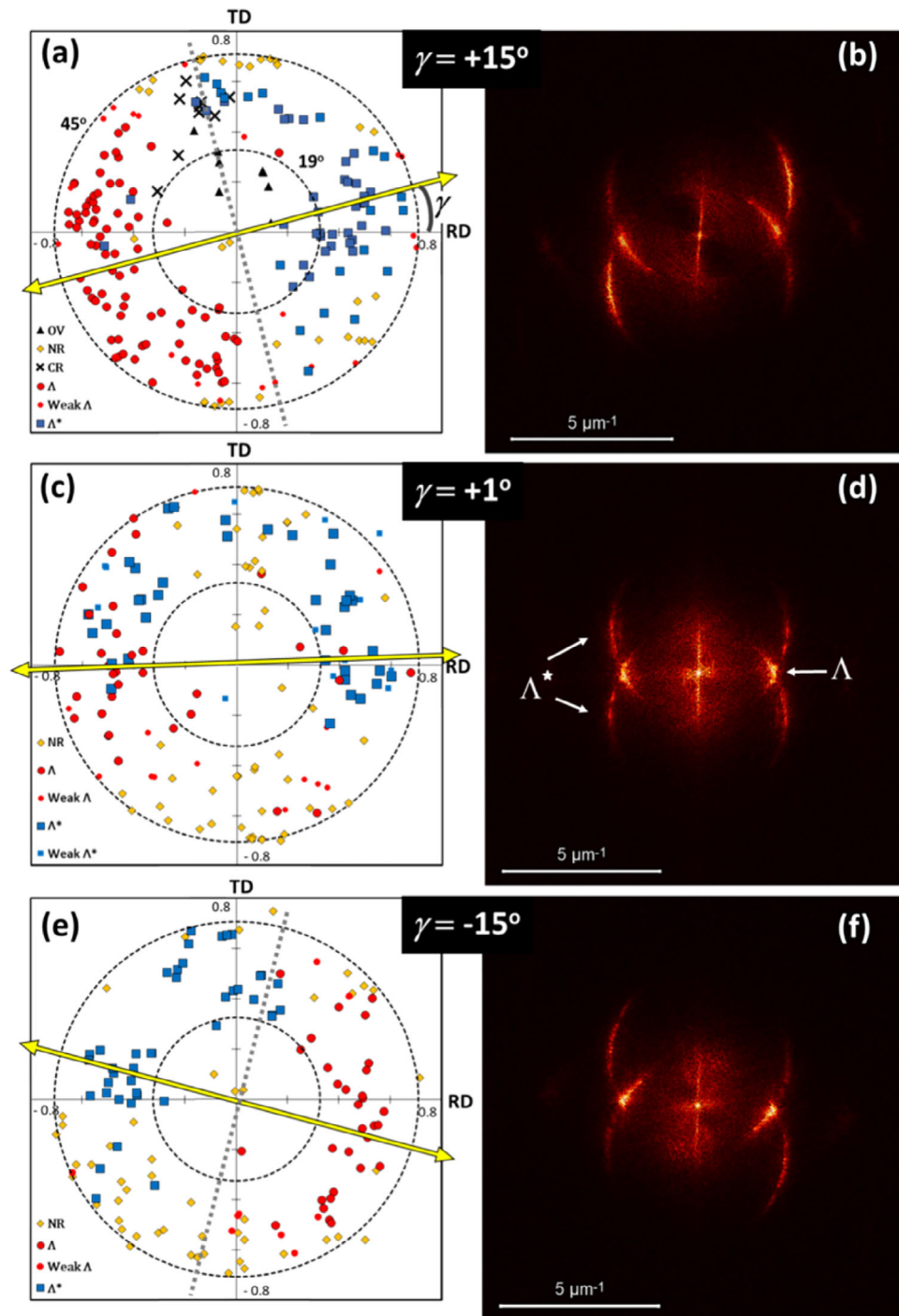$$RD_i = \cos(E1_i + 270) * X \tag{A2}$$

$$TD_i = \sin(E1_i + 270) * X$$

In units of e, the projections can be calculated as:

$$RD_i = \cos(E1_i + 270) * \cos(90 - E2_i) \tag{A4}$$

$$TD_i = \sin(E1_i + 270) * \cos(90 - E2_i)$$

Following these calculations, each grain at the surface is represented in this 2D-Cartesian system by a point (RD_i, TD_i), whose associated vector is $\vec{X}$: $E1_i$ determines the angle of this vector, and $E2_i$ is related to its modulus (see Figure A1f).

Appendix B

Figure B1. a,c,e) RD-TD grain orientation (left column) maps and b,d,f) 2D-FFT images (right column) obtained for samples after laser treatments $\alpha = \theta = 30°$ and s-polarization with deviation angles $\gamma = +15°$ (T30s), $+1°$ and $-15°$. Each symbol corresponds to an analyzed grain, whose (TD_i, RD_i) components have been calculated using Equation (A4). The axes values are given in units of e and the circumferences correspond to fixed $E2_i$ values as indicated (see Figure A1). The different symbols correspond to the type of nanostructure observed for each grain (see Figures 1, 3, and 4): Ov (overtreated); NR (no-ripples); Λ or Λ^* (ripples); CR (cross ripples). The yellow double-arrows represent the laser PD projection on the RD-TD plane. The dotted line is the direction perpendicular to PD.
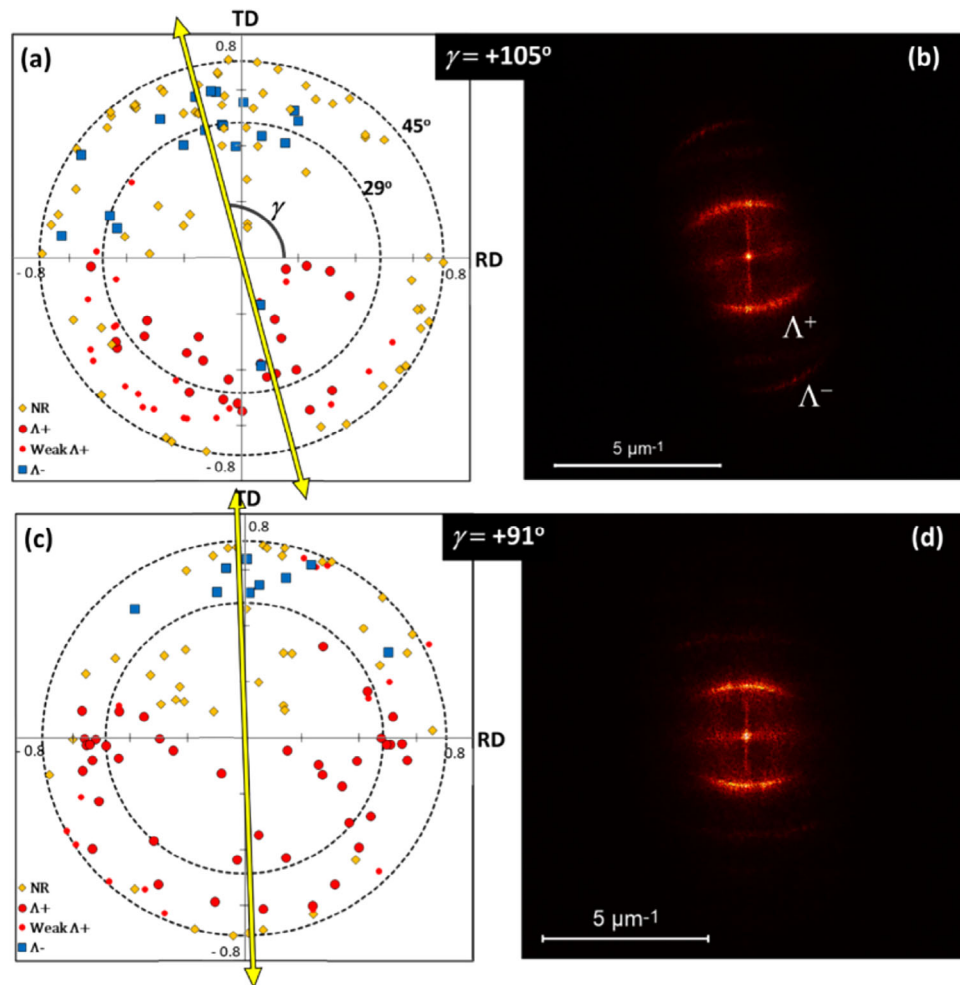
Figure B2. a,c) RD-TD grain orientation (left column) maps and b,d) 2D-FFT images (right column) obtained for samples after laser treatments $\alpha = \theta = 30°$ and p-polarization with angles $\gamma = +105°$ (T30p) and $+91°$. Each symbol corresponds to an analyzed grain, whose (TD_i, RD_i) components have been calculated using Equation (A4). The axes values are given in units of e and the circumferences correspond to fixed $E2_i$ values as indicated (see Figure A1). The different symbols correspond to the type of nanostructure observed for each grain (see Figures 1, 3, and 5): Ov (overtreated); NR (no-ripples); Λ^+ or Λ^- (ripples); CR (cross ripples). The yellow double-arrows represent the laser PD projection on the RD-TD plane. Λ^- ripples are barely visible in (d).

Appendix C
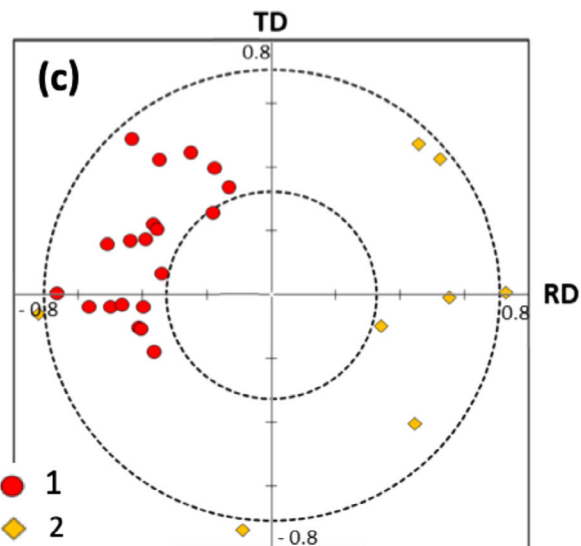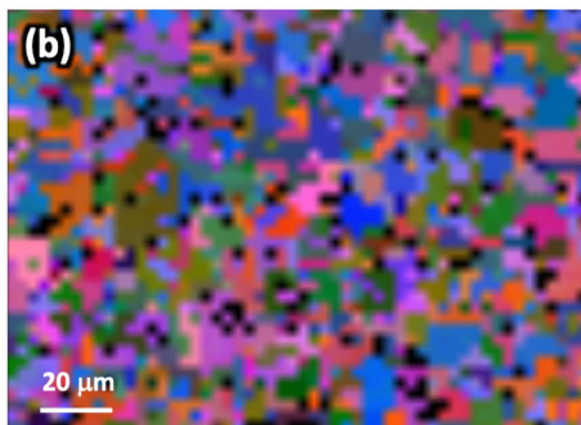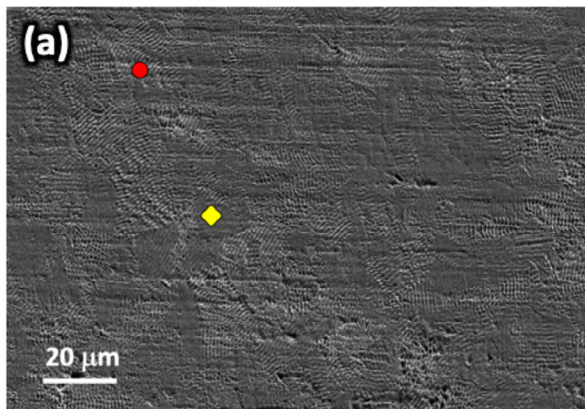
Figure C1. a) SEM micrograph (SE) of a SS316L surface treated with an 800 ps IR ($\lambda = 1064$ nm) laser (sample was tilted at $\alpha = 70°$ for EBSD analysis). The laser processing parameters are: $f_{rep} = 300$ kHz, $E_{pulse} = 14.7$ µJ, $v_{laser} = 1500$ mm s^{-1} and $\delta_{lines} = 3$ µm. b) EBSD Euler map of the same area. c) RD-TD grain orientation map. Each symbol corresponds to an analyzed grain showing well-defined ripples ($\Lambda \approx 1$ µm) (Nanostructure type 1) or a nanostructure with emerging ripples (Nanostructure type 2). The axes values are given in units of e.

Conflict of Interest

The authors declare no conflict of interest.

Data Availability Statement

The data that support the findings of this study are openly available in [ZENODO] at [https://doi.org/10.5281/zenodo.8081667], reference number [8081667].

[1] A. Bekmurzayeva, W. J. Duncanson, H. S. Azevedo, D. Kanayeva, *Mater. Sci. Eng. C* **2018**, *93*, 1073.
[2] W. Frediksson, Ph.D thesis, Uppsala University, **2012**.
[3] Q. Chen, G. A. Thouas, *Mater. Sci. Eng. R* **2015**, *87*, 1.
[4] J. Hasan, R. J. Crawford, E. P. Ivanova, *Trends Biotechnol.* **2013**, *31*, 295.
[5] H. Hermawan, D. Ramdan, J. R. Djuansjah, in *Biomedical Engineering - From Theory to Applications*, (Ed.: R. Fazel-Rezai), InTechOpen, London **2011**.
[6] A. H. A. Lutey, L. Gemini, L. Romoli, G. Lazzini, F. Fuso, M. Faucon, R. Kling, *Sci. Rep.* **2018**, *8*, 10112.
[7] J. Bonse, S. V. Kirner, J. Krüger, in *Handbook of Laser Micro- and Nano-Engineering*, (Ed.: K. Sugioka), Springer, Cham **2021**.
[8] J. Bonse, S. Hohm, S. V. Kirner, A. Rosenfeld, J. Kruger, *IEEE J. Sel. Top. Quant. Electron.* **2017**, *23*, 9000615.
[9] J. Bonse, S. Gräf, *Nanomaterials* **2021**, *11*, 3326.
[10] J. Bonse, S. Gräf, *Laser Photonics Rev.* **2021**, *14*, 2000215.
[11] J. Bonse, A. Rosenfeld, J. Krüger, *J. Appl. Phys.* **2009**, *106*, 104910.
[12] Z. Guosheng, P. M. Fauchet, A. E. Siegman, *Phys. Rev. B* **1982**, *23*, 5366.
[13] D. Bäuerle, in *Laser Processing and Chemistry*, Springer-Verlag, Berlin **2011**, p. 626.
[14] A. M. Bonch-Bruevich, *Opt. Eng.* **1992**, *31*, 718.
[15] T. Y. Hwang, C. Guo, *J. Appl. Phys.* **2010**, *108*, 073523.
[16] P. Nürnberger, H. Reinhardt, H.-C. Kim, F. Yang, K. Peppler, J. Janek, N. Hampp, *J. Appl. Phys.* **2015**, *118*, 134306.
[17] Y. Fuentes-Edfuf, J. A. Sánchez-Gil, M. Garcia-Pardo, R. Serna, G. D. Tsibidis, V. Giannini, J. Solis, J. Siegel, *Appl. Surf. Sci.* **2019**, *493*, 948.
[18] S. Maragkaki, C. A. Skaradzinski, R. Nett, E. L. Gurevich, *Sci. Rep.* **2020**, *10*, 53.

[19] L. Porta-Velilla, N. Turan, Á. Cubero, W. Shao, H. Li, G. F. De La Fuente, E. Martínez, Á. Larrea, M. Castro, H. Koralay, S. K. Çavdar, J. Bonse, L. A. Angurel, *Nanomaterials* **2022**, *12*, 2380.

[20] V. Lennikov, B. Özkurt, L. A. Angurel, A. Sotelo, B. Özçelik, G. F. De La Fuente, *J. Supercond. Nov. Magn.* **2013**, *26*, 947.

[21] A. Cubero, E. Martínez, L. A. Angurel, G. F. De La Fuente, R. Navarro, H. Legall, J. Krüger, J. Bonse, *Appl. Surf. Sci.* **2020**, *508*, 145140.

[22] G. R. B. E. Römer, A. J. Huis In't Veld, J. Meijer, M. N. W. Groenendijk, *CIRP Ann.-Manuf. Technol.* **2009**, *58*, 201.

[23] X. Sedao, C. Maurice, F. Garrelie, J.-P. Colombier, S. Reynaud, R. Quey, F. Pigeon, *Appl. Phys. Lett.* **2014**, *104*, 171605.

[24] G. Giannuzzi, C. Gaudiuso, R. Di Mundo, L. Mirenghi, F. Fraggelakis, R. Kling, P. M. Lugarà, A. Ancona, *Appl. Surf. Sci.* **2019**, *494*, 1055.

[25] B. Karlsson, C. G. Ribbing, *J. Appl. Phys.* **1982**, *53*, 6340.

[26] T. J.-Y. Derrien, J. Krüger, J. Bonse, *J. Opt.* **2016**, *18*, 115007.

[27] K. Sokolowski-Tinten, J. Bonse, A. Barty, H. N. Chapman, S. Balt, M. J. Bogan, S. Boutet, A. Cavalleri, S. Düsterer, M. Frank, J. Hajdu, S. Hau-Riege, S. Marchesini, N. Stojanovic, R. Treusch, in *Ultrafast Laser Nanostructuring – The Pursuit of Extreme Scales*, (Eds.: R. Stoian, J. Bonse), Springer, Cham **2023**.

[28] J. E. Sipe, J. F. Young, J. S. Preston, H. M. Van Driel, *Phys. Rev. B* **1983**, *27*, 1141.

[29] J. Bonse, M. Munz, H. Sturm, *J. Appl. Phys.* **2005**, *97*, 013538.

[30] A. Siegman, P. Fauchet, *IEEE J. Quant. Electron.* **1986**, *22*, 1384.

[31] J. F. Young, J. S. Preston, H. M. Van Driel, J. E. Sipe, *Phys. Rev. B* **1983**, *27*, 1155.

[32] J. M. Liu, *Opt. Lett.* **1982**, *7*, 196.

[33] K. M. Lecka, A. J. Antonczak, B. Szubzda, M. R. Wójcik, B. D. Stepak, P. Szymczyk, M. Trzcinski, M. Ozimek, K. M. Abramski, *J. Laser Appl.* **2016**, *28*, 032009.